CrossMark

J/M PAPERS

Low-Reynolds-number oscillating boundary layers on adiabatic slopes

Bryan E. Kaiser[1],[†], Lawrence J. Pratt[2] and Jörn Callies[3]

[1]Los Alamos National Laboratory, Los Alamos, NM 87545, USA

[2]Woods Hole Oceanographic Institution, Woods Hole, MA 02543, USA

[3]Caltech, Pasadena, CA 91125, USA

We investigate the instabilities and transition mechanisms of Boussinesq stratified boundary layers on sloping boundaries when subjected to oscillatory body forcing parallel to the slope. We examine idealized forms of boundary layers on hydraulically smooth abyssal slopes in tranquil mid- to low-latitude regions, where low-wavenumber internal tides gently heave isopycnals up and down adiabatic slopes in the absence of mean flows, high-wavenumber internal tides, shelf breaks, resonant tide–bathymetry interactions (critical slopes) and other phenomena associated with turbulence 'hot spots'. In non-rotating low-Reynolds-number flow, increased stratification on the downslope phase has a relaminarizing effect, while on the upslope phase we find transition-to-turbulence pathways arise from shear production triggered by gravitational instabilities. When rotation is significant (low slope Burger numbers) we find that boundary layer turbulence is sustained throughout the oscillation period, resembling stratified Stokes–Ekman layer turbulence. Simulation results suggest that oscillating boundary layers on smooth slopes at low Reynolds number ($Re \leqslant 840$), unity Prandtl number and slope Burger numbers greater than unity do not cause significant irreversible turbulent buoyancy flux (mixing), and that flat-bottom dissipation rate models derived from the tide amplitude are accurate within an order of magnitude.

Key words: boundary layer stability, buoyancy-driven instability, stratified flows

1. Introduction

Irreversible buoyancy flux convergence within oscillating stratified boundary layers on sloping bathymetry in the abyss may be a significant mechanism driving the deep branch of the global overturning circulation (Ferrari *et al.* 2016). The boundary layers, combined with other bottom-intensified sources of turbulence, such as the breaking of internal

† Email address for correspondence: bkaiser@lanl.gov

950 A4-1

waves, contribute to observed patterns of intense irreversible buoyancy flux convergence (Polzin 1996) at turbulence 'hot spots' (Thorpe 2007). However, little is known about the laminar, transitional and turbulent processes on gently sloping smooth bathymetry in the 'tranquil regions' (Angel 1990) of the abyssal ocean. One example of a tranquil region slope is at $34°N$ $70°W$, where the northwest edge of the Sargasso Sea meets the deep end of the continental slope. Modelled maximum (spring tide) tidal current velocities near the seafloor (Turnewitsch *et al.* 2013), assessments of slope criticality (Becker & Sandwell 2008) and abyssal mooring observations (Tarbell, Montgomery & Briscoe 1985; Nash *et al.* 2004) at that location suggest 'tranquil region' boundary layers characterized by subcritical slopes, tide velocity amplitudes of less than or approximately equal to 0.01 m s^{-1} and boundary layer thicknesses of $O(10)$ m.

How unstable are tranquil region boundary layers on abyssal slopes, and what are the instability mechanisms? In this article, we employ theory and simulations to investigate the pathways between laminar, transitional and turbulent states of boundary layers that are forced by the M_2 barotropic tide and occur on hydraulically smooth abyssal slopes in the absence of forcing by high-wavenumber internal waves, mean flows, far-field turbulence on larger scales and resonant tidal–bathymetric interaction. Although tranquil region abyssal slopes are typically subcritical (Becker & Sandwell 2008), we extend our analyses to supercritical slopes for completeness.

The boundary layers are formed as momentum and buoyancy are diffused by no-slip and adiabatic boundary conditions on sloping bathymetry as low-wavenumber internal waves heave isopycnals (constant-density contours) up and down slopes. Figure 1 illustrates the scale separations between the horizontal length scale of bathymetric features such as continental slopes, k^{-1}, the excursion length scale of the tide, L, and the largest boundary layer length scale, δ_l. The excursion length scale, L, is the characteristic scale of the across-isobath distance between the trajectory extrema in the inviscid problem, defined as

$$L \sim \frac{U_\infty}{\omega}, \tag{1.1}$$

where U_∞ is the barotropic tide amplitude projected onto the across-slope tangential coordinate (x) and ω is the tide frequency. We assume that the slope is reasonably approximated as constant on scales of the order of the excursion length, L. Thus the boundary layers investigated in this article apply to boundary layer flows on hydraulically smooth slopes where the excursion parameter

$$\mathcal{E} = kL \tag{1.2}$$

is small, $\mathcal{E} \ll 1$. The excursion parameter $\mathcal{E}$ is the ratio of net fluid advection by the barotropic tide to the topographic length. The baroclinic response to the barotropic forcing is highly nonlinear for large-excursion-parameter flows $\mathcal{E}$ (Bell 1975*a*,*b*; Garrett & Kunze 2007; Sarkar & Scotti 2017). Here, we investigate the dynamics on scales at or smaller than the excursion length; thus we assume that the baroclinic tide (or internal waves) generated by bathymetric features with horizontal length scales of k^{-1} can be locally approximated as irrotational over $L \sim O(100)$ m. Therefore we model low-wavenumber baroclinic tides, or any oscillatory forcing occurring at frequencies in the range $f < \omega < N$ and characterized by vertical and horizontal structure that can be reasonably approximated as spatially homogeneous over length scales $O(10)$ m, as an across-isobath oscillating body force.

Non-rotating, large-angle ($42°$), low-*Re* experiments by Hart (1971) showed that, when $\omega^2 \ll N^2$, 'plumes' form during the upward boundary layer flow phase that are mixed
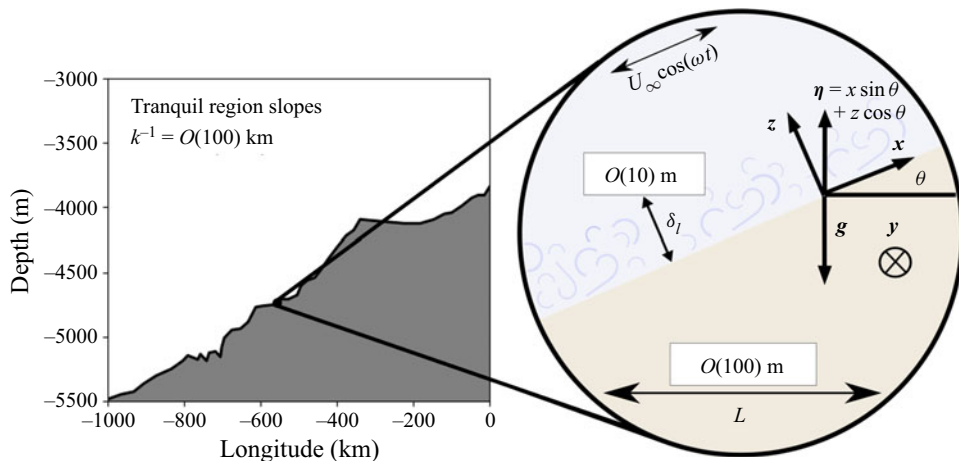
Figure 1. Illustration of boundary layers in tranquil abyssal regions at the deep end of a continental slope. The heaving of density surfaces up and down the slope by oscillations with vertical and horizontal structure characterized by length scales much greater than $O(10)$ m creates an oscillating boundary layer.

and stabilized during the downslope phase. Our objectives are (1) to determine if these boundary layers are laminar, transitional, intermittent or fully turbulent for a range of parameters that include those typical of abyssal ocean non-dimensional parameters associated with the M_2 tide, (2) to investigate the transition mechanisms and (3) to test back-of-the-envelope estimation for barotropic tide dissipation rates at the seafloor. The rest of this article is organized as follows. In § 2 we discuss the relevant governing equations and non-dimensional parameters. In § 3 we investigate analytical solutions for the laminar flows to estimate the necessary conditions for boundary layer gravitational instabilities. In § 4 we analyse the stability of simulated boundary layers and in § 5 we summarize the observed transition mechanisms and drag coefficients.

2. Problem formulation

The flows examined in this study are subject to a body force in the across-isobath, or streamwise, direction (the x direction in figure 1):

$$F_d(t_d) = -\text{Re}[A_d e^{i\omega t_d}], \qquad (2.1)$$

where A_d is the dimensional amplitude of the pressure gradient $\partial_x \tilde{P}_d$ and t_d is dimensional time.

Several geometric and physical approximations are invoked for the sake of tractibility and conceptual simplicity. The flow is approximated as Boussinesq: the density variations are small enough that the incompressibility condition is justified, and Joule heating (increases of internal energy due to the viscous dissipation of mechanical energy) is neglected. We idealize abyssal buoyancy as a linear function of temperature alone.

A Cartesian coordinate system, rotated θ radians counterclockwise above the horizontal (figure 1), was chosen for analytical convenience. The z coordinate is the wall-normal (or transverse) coordinate, which is at angle θ from the vertical coordinate (the coordinate anti-parallel to gravity). To distinguish between the slope-normal and vertical coordinates, the vertical coordinate (and vertical velocities, fluxes, etc.) in the direction normal to Earth's surface will be denoted as η, such that $\eta = x \sin \theta + z \cos \theta$, shown in figure 1.

The non-dimensional Boussinesq governing equations for conservation of mass, momentum and thermodynamic energy for the flow are

$$\partial_x \tilde{u} + \partial_y \tilde{v} + \partial_z \tilde{w} = 0, \tag{2.2}$$

$$d_t \tilde{u} = \frac{1}{Ro} \tilde{v} - \partial_x \tilde{p} + \frac{1}{Re_L} \left(\partial_{xx} + \partial_{yy} + \partial_{zz} \right) \tilde{u} + C^2 \tilde{b} + F(t), \tag{2.3}$$

$$d_t \tilde{v} = -\frac{1}{Ro} \tilde{u} - \partial_y \tilde{p} + \frac{1}{Re_L} \left(\partial_{xx} + \partial_{yy} + \partial_{zz} \right) \tilde{v}, \tag{2.4}$$

$$d_t \tilde{w} = -\partial_z \tilde{p} + \frac{1}{Re_L} \left(\partial_{xx} + \partial_{yy} + \partial_{zz} \right) \tilde{w} + C^2 \tilde{b} \cot \theta, \tag{2.5}$$

$$d_t \tilde{b} = \frac{1}{Pr \, Re_L} \left(\partial_{xx} + \partial_{yy} + \partial_{zz} \right) \tilde{b}, \tag{2.6}$$

where $d_t = \partial_t + \tilde{\boldsymbol{u}} \cdot \nabla$ and $F(t) = F_d(t_d)/(U_\infty \omega) = A \sin(t)$. The variables are non-dimensionalized as follows (subscript 'd' denoting dimensional variables):

$$x = x_d/L, \quad \tilde{\boldsymbol{u}} = \tilde{\boldsymbol{u}}_d/U_\infty, \quad t = \omega t_d, \quad \tilde{p} = \tilde{p}_d/U_\infty^2, \quad \tilde{b} = \tilde{b}_d/(LN^2 \sin \theta), \quad (2.7a\text{--}e)$$

where the reference density ρ_0 is absorbed into the mechanical pressure p_d such that it has units of J kg^{-1}. Parameter N^2 is the square of the buoyancy frequency (the natural frequency associated with the restoring force of stratification). The buoyancy is defined as the acceleration associated with density anomalies, $b_d = g(\rho_0 - \rho)/\rho_0$, where g is the (constant) gravity and ρ is the density.

Despite the assumptions and idealizations listed above, the dynamical parameter space is vast. The relevant non-dimensional ratios are the Prandtl number Pr, the slope Rossby number Ro, the slope frequency ratio C and Stokes layer Reynolds number Re. In this study, the Stokes layer Reynolds number is referred to in the analysis of the flow instead of the excursion length Reynolds number,

$$Re_L = \frac{U_\infty L}{\nu} = \frac{U_\infty^2}{\nu \omega}, \tag{2.8}$$

because the Stokes layer Reynolds number is common in literature regarding oscillating boundary layers. The Prandtl and Stokes layer Reynolds numbers are defined as

$$Pr = \frac{\nu}{\kappa}, \tag{2.9}$$

$$Re = \frac{U_\infty \delta}{\nu} = \sqrt{2 Re_L}, \tag{2.10}$$

where κ is the molecular diffusivity of buoyancy and ν is the kinematic viscosity of abyssal seawater, and where the Stokes layer thickness is

$$\delta = \sqrt{2\nu/\omega}. \tag{2.11}$$

The slope frequency ratio is defined as the ratio of the projection of the buoyant acceleration onto the across-slope (x) direction (parallel to the forcing) to the acceleration of the oscillatory forcing:

$$C = \frac{N \sin \theta}{\omega}. \tag{2.12}$$

The slope frequency ratio was first identified as an important ratio for describing the boundary layer by Hart (1971) (who denoted it as Q, where $Q = C^2$), while the frequency

ratio N/ω emerges as an important measure of the role of stratification in the stratified form of Stokes' second problem (Gayen & Sarkar 2010*a*). The slope frequency ratio is indicative of the degree of resonance between the oscillation body forcing and the buoyant restoring force.

Finally, the fourth non-dimensional ratio is the slope Rossby number:

$$Ro = \frac{\omega}{f \cos \theta}, \tag{2.13}$$

which indicates the ratio of the influence of planetary vorticity (projected onto the wall-normal direction) relative to vorticity with a characteristic time scale of the tide period, ω^{-1}. For the finite-Rossby-number cases examined, ω is the M_2 tide frequency, the Coriolis parameter, f, is 10^{-4} s^{-1} and the range of slope angles investigated are within $0 < \theta \leqslant 14°$. Therefore, the slope Rossby number is approximately 1.4 for all of the rotating reference frame flows investigated.

2.1. *Inviscid, linear flow*

The inviscid, linearized forms of the governing equations (2.2)–(2.6) describe the heaving of isopycnals up and down the slope:

$$\partial_t \tilde{u} = \frac{1}{Ro} \tilde{v} + C^2 \tilde{b} + F(t), \tag{2.14}$$

$$\partial_t \tilde{v} = -\frac{1}{Ro} \tilde{u}, \tag{2.15}$$

$$\partial_t \tilde{b} = -\tilde{u}. \tag{2.16}$$

Crucially, the solutions to (2.14)–(2.16) prescribe the amplitude of the non-dimensional body force:

$$A = \left(C^2 + \frac{1}{Ro^2} - 1 \right), \tag{2.17}$$

where $A_d = A U_\infty \omega$. The solutions to (2.16)–(2.16) are

$$\tilde{u}(t) = -\cos(t), \tag{2.18}$$

$$\tilde{v}(t) = Ro^{-1} \sin(t), \tag{2.19}$$

$$\tilde{b}(t) = \sin(t). \tag{2.20}$$

2.2. *Resonance*

The assumption that the vertical and horizontal structure of an internal wave is constant over a length scale of $O(10)$ m is not valid if the wave is critical. At critical slope, the forcing model $F(t)$ in (2.1) and (2.14) is degenerate and vanishes if the critical slope condition

$$C^2 + \frac{1}{Ro^2} - 1 = 0 \tag{2.21}$$

is satisfied. If (2.21) is satisfied, the energy of the inviscid baroclinic tide is tightly focused into narrow beams that follow the curvature of the bathymetry (Balmforth, Ierley & Young 2002).

Equation (2.21) is formally consistent with internal wave theory. In internal wave theory, critical slopes are defined by

$$\tan \theta_c = \sqrt{\frac{\omega^2 - f^2}{N^2 - \omega^2}}, \qquad (2.22)$$

where θ_c is the critical slope angle. If the slope angle $\theta \neq \theta_c$, then (2.17) is satisfied, $A \neq 0$. Equation (2.17) can be rearranged to obtain

$$\tan \theta = \sqrt{\frac{\omega^2 (1 + A) - f^2}{N^2 - \omega^2 (1 + A)}}. \qquad (2.23)$$

Therefore the criticality condition in (2.21) is just a rearrangement of the criticality condition defined by the slope parameter ϵ from internal wave theory:

$$\epsilon = \frac{\tan \theta}{\tan \theta_c}, \qquad (2.24)$$

where criticality states are defined:

$$\left. \begin{array}{llllll} \text{if} & A < 0 & \text{then} & \epsilon < 1 & \rightarrow & \theta \text{ is subcritical,} \\ \text{if} & A = 0 & \text{then} & \epsilon = 1 & \rightarrow & \theta \text{ is critical,} \\ \text{if} & A > 0 & \text{then} & \epsilon > 1 & \rightarrow & \theta \text{ is supercritical.} \end{array} \right\} \qquad (2.25)$$

2.3. *Boundary conditions*

At the solid boundary at $z = 0$, the boundary conditions on the total velocity are no-slip and impermeability

$$\tilde{\boldsymbol{u}} = 0, \qquad (2.26)$$

and the boundary conditions on the total buoyancy is the adiabatic condition:

$$\partial_z \tilde{b} = 0. \qquad (2.27)$$

As $z \rightarrow \infty$, the velocity boundary conditions are the oscillatory solutions for the inviscid flow, and zero flow in the wall-normal direction: (2.18), (2.19) and $\widetilde{w} = 0$. The non-dimensional buoyancy field as $z \rightarrow \infty$ has two components, the inviscid oscillation and the constant background stratification:

$$\tilde{b} = x + z \cot \theta + \sin(t). \qquad (2.28)$$

2.4. *Variable decomposition*

The total velocity and buoyancy fields are decomposed into three components that when summed together satisfy (2.2)–(2.6) and (2.26)–(2.28). To distinguish the components, let 'H' denote the hydrostatic (and possibly geostrophic) component, let 'S' denote the steady component and let 'O' denote the oscillating component:

$$\tilde{\boldsymbol{u}}(x, y, z, t) = \boldsymbol{u}_H + \boldsymbol{u}_S(z) + \boldsymbol{u}_O(x, y, z, t), \qquad (2.29)$$

$$\tilde{b}(x, y, z, t) = b_H(x, z) + b_S(z) + b_O(x, y, z, t), \qquad (2.30)$$

$$\tilde{p}(x, y, z, t) = p_H(x, z) + p_S(z) + p_O(x, y, z, t). \qquad (2.31)$$

The hydrostatic component of the buoyancy field is merely the background stratification in the rotated coordinate system, $b_{H,d}(x_d, z_d) = N^2 (x_d \sin \theta + z_d \cos \theta)$ in dimensional

950 A4-6

form, and the quiescent hydrostatic velocity field $\boldsymbol{u}_H = 0$ everywhere except in the finite-Rossby-number flow regime, in which case it is the along-slope geostrophic velocity that arises from the across-isobath pressure gradient imposed by the slope (Phillips 1970; Wunsch 1970). The buoyancy frequency N is defined in the same manner as convention:

$$N^2 = -\frac{g}{\rho_0}\partial_\eta \rho_H = \partial_\eta b_{H,d}, \tag{2.32}$$

where η denotes the vertical position coordinate as shown in figure 1.

The steady and oscillating flow components are anomalies from the hydrostatic background that ensure the satisfaction of frictional and diffusive boundary conditions at the wall and inviscid oscillations far from the wall. It is convenient to solve for the anomalies,

$$\boldsymbol{u}(x, y, z, t) = \boldsymbol{u}_S(z) + \boldsymbol{u}_O(x, y, z, t), \tag{2.33}$$

$$b(x, y, z, t) = b_S(z) + b_O(x, y, z, t), \tag{2.34}$$

$$p(x, y, z, t) = p_S(z) + p_O(x, y, z, t), \tag{2.35}$$

because the removal of the hydrostatic background permits periodic analytical and numerical solutions for $\boldsymbol{u}$ and b.

3. Linear solutions

Analytical solutions to linearized forms of (2.2)–(2.6) contain a wealth of information pertaining to the laminar, disturbed laminar and intermittently turbulent regimes (i.e. low- to moderate-Reynolds-number flows) that are investigated numerically in this study. Thorpe (1987) provided solutions of the rotating linear problem, a detailed derivation of which is given in Appendix A. The solutions in Appendix A are written in a form that readily collapses in the $Ro \to \infty$ regime.

3.1. *Necessary conditions for gravitational instability*

The linear solutions for the steady flow component of both rotating and non-rotating flows is always gravitationally stable, meaning that the total vertical buoyancy gradient is never negative,

$$\partial_\eta b_H + \partial_\eta b_S = 1 - \cos^2\theta e^{-\eta/\delta_S}\sqrt{2}\sin\left(\frac{\eta}{\delta_S} + \frac{\pi}{4}\right) \geqslant 0, \tag{3.1}$$

if the oscillating component vanishes. The boundary layer thickness of the steady component (Phillips 1970; Wunsch 1970) is

$$\delta_S = \left(\frac{f^2\cos^2\theta}{4\nu^2} + Pr\frac{N^2\sin^2\theta}{4\nu^2}\right)^{-1/4}. \tag{3.2}$$

The oscillating flow component solutions exhibit transient gravitationally unstable buoyancy gradients, $\delta_\eta \tilde{b} < 0$, when denser fluid is advected over lighter fluid during portions of the oscillation period. If the oscillating component is non-zero, then the minimum necessary condition for gravitational instabilities is defined by

$$\partial_\eta b_H + \partial_\eta b_S < -\partial_\eta b_O, \tag{3.3}$$

because if (3.3) is satisfied, then the total vertical buoyancy gradient is negative, $\delta_\eta \tilde{b} < 0$. However, instabilities can grow only if the negative buoyancy gradient is sustained for a significant amount of time and if it is negative enough to overcome resistance from friction.
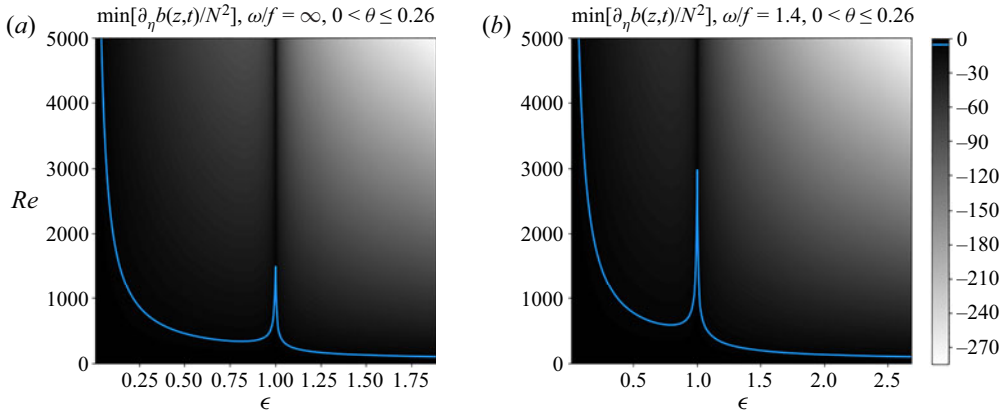
Figure 2. Total buoyancy gradient minima. The minimum value (in both time and space) of the non-dimensional linear solution vertical buoyancy gradient for (*a*) the non-rotating reference frame case ($f = 0$) and (*b*) the rotating reference frame case.

A characteristic boundary layer Rayleigh number and a ratio of the time scale of the growth of an instability to the period of the oscillation are required to estimate the minimum (quasi-steady) conditions for the growth of gravitational instabilities. However, the linear solutions do not readily yield a single boundary layer buoyancy gradient length scale. If the buoyancy gradient length scale is assumed to scale with $\delta = \sqrt{2\nu/\omega}$, then a tenable time-dependent boundary layer Rayleigh number is defined:

$$Ra(t) \sim \frac{4PrN^2}{\omega^2}\partial_\eta \tilde{b}(t), \tag{3.4}$$

which only applies when $\partial_\eta \tilde{b}(t) < 0$. To estimate the gravitational stability of the flow without explicitly accounting for the time dependence of the basic state (the quasi-steady assumption), the basic state of the flow cannot change more rapidly than the growth rate of a gravitational instability. If the instabilities are 'slowly modulated' by the basic state (Davis 1976), the quasi-steady assumption is reasonable for stability analysis. The dimensional instantaneous growth rate of a gravitational instability can be estimated as

$$\sigma \sim \mathrm{Im}\left[\sqrt{\partial_\eta \tilde{b}N^2}\right]. \tag{3.5}$$

If $|\omega/\sigma| \ll 1$, then the modulation by the basic state is sufficiently slow for the growth of gravitational instabilities.

Figure 2 shows the minimum values of the non-dimensional total vertical buoyancy gradient from the linear solutions for non-rotating and rotating cases as a function of slope parameter and Stokes Reynolds number. Assuming that the gravitational instability in the boundary layer is physically similar to that of Rayleigh–Bénard instability in the case of one rigid and one stress-free boundary, then the critical Rayleigh number for the boundary layer is $Ra_c \approx 1100$ (Chandrasekhar 1961), which corresponds to $|\omega/\sigma| = 0.06$. For the chosen fluid properties (holding $Pr = 1, f = 10^{-4}, N = 10^{-3}$ and $\omega = 1.4 \times 10^{-4}$ constant), $Ra_c \approx 1100$ corresponds to a critical non-dimensional vertical buoyancy gradient of $\partial_\eta \tilde{b} = -5.4$, which is shown as the blue lines in figure 2. The minimum boundary layer buoyancy gradient is less than zero for all non-zero Re and ϵ, and the minimum boundary layer buoyancy gradient is increasingly negative with increasing

950 A4-8

Cases	Re	Ro	C	ϵ	θ (rad)
1, 9	840, 420	∞	0.25	0.25	3.53×10^{-2}
2, 10	840, 420	∞	0.75	0.75	1.06×10^{-1}
3, 11	840, 420	∞	1.25	1.25	1.76×10^{-1}
4, 12	840, 420	∞	1.75	1.75	2.47×10^{-1}
5, 13	840, 420	1.41	0.25	0.35	3.53×10^{-2}
6, 14	840, 420	1.41	0.75	1.06	1.06×10^{-1}
7, 15	840, 420	1.43	1.25	1.79	1.76×10^{-1}
8, 16	840, 420	1.45	1.75	2.53	2.47×10^{-1}

Table 1. Prescribed non-dimensional simulation parameters. The four independent parameters are Re, Ro, C, θ, where $Pr = 1$ is not varied. The slope parameter $\epsilon = \tan\theta / \tan\theta_c$ is also used in this study to directly connect results to internal wave parameters. The slope Burger number is $Bu = N^2 \tan^2\theta / f^2 = Ro^2 C^2$.

Reynolds number and with increasing slope parameter. The discontinuity at $\epsilon = 1$ is an artefact of the degeneracy of linear solutions at critical slope. The ϵ axis between the non-rotating and rotating cases is different because rotation alters the angle of critical slope; both plots show the same slope angle range, $0 < \theta \leqslant 16°$.

4. Nonlinear solutions

In this section we examine the nonlinear stability and development of turbulence in boundary layers on smooth abyssal slopes for both rotating and non-rotating regimes. The boundary layers are initialized by the oscillating laminar flow solutions derived in Appendix A. We varied the slope Rossby number (nearly constant with slope, (2.13)), slope frequency ratio (2.12), Reynolds number (2.10), slope parameter (2.24) and slope angle θ for each of the 16 simulations as shown in table 1. The slope frequency ratio C and slope parameter ϵ are redundant for the non-rotating case, but are shown together because $C \neq \epsilon$ for the rotating flow, and C appears explicitly in the forcing of the across-isobath (x) momentum equation. We observed bursts of turbulence, triggered by two-dimensional gravitational instabilities that rapidly become three-dimensional, during the upslope flow phase of all cases at $Re = 840$ except for the case of lowest slope Burger number, which exhibits turbulence sustained throughout the period. At $Re = 420$, the flow matched the laminar analytical solutions except for weak turbulent bursts that occurred at the highest slope angles in the rotating regime.

4.1. *Numerical implementation*

The flow anomalies, as defined by (2.33) and (2.34), are discretized to satisfy periodic boundary conditions in the wall-parallel directions via Fourier spectral bases in the across-isobath (x) and along-isobath (y) directions. Periodicity is not merely numerically convenient; it also eliminates the need to prescribe buoyancy forcing ('restratification') because the oscillating flow can advect the background field to gain or lose buoyancy. In the periodic domain, the boundary layer buoyancy can only reach a homogenized steady state if the turbulence sustainably converts tidal momentum to potential energy throughout the entire period.

Although the planar extent of the computational domain is less than the excursion length of the tide, the domain size (table 2) is justifiably sufficient because the largest eddies in oscillating boundary layers are those associated with the transverse (wall-normal) length scale, which is much less than the excursion length. Indeed, at higher Reynolds number

Re	$(L_x, L_y)/\delta$	H/δ	$(\Delta x^+, \Delta y^+)$	Δz_{wall}^+	$(\Delta x, \Delta y)/l_K$	$\Delta z_{wall}/l_K$	$\Delta t_d/\tau_K$	$\Delta t_d/T$
420	59.3	177.8	9.5	0.69	13.8	0.40	0.01	2.2×10^{-5}
840	59.3	177.8	13.5	0.97	18.0	0.52	0.02	2.2×10^{-5}

Table 2. Resolution parameters. The grid is identical in the x and y directions. Kolmogorov scales are estimated assuming that the law of the wall holds; therefore, characteristic dissipation rate is estimated *a priori* by $\varepsilon \sim U_*^3/(\delta\kappa_*)$, where the von Kármán constant is $\kappa_* = 0.41$ and the friction velocity is estimated by $U_* \sim \sqrt{\nu U_\infty/\delta}$.

($Re = 1790$), Gayen & Sarkar (2010*b*) found the turbulent boundary layer thickness, δ_l, was $\delta_l = 15\delta$ for the unstratified problem and $\delta_l = 17\delta$ for flat-plate stratified oscillating boundary layers at the same Reynolds number. The grid resolution parameters for the two Reynolds numbers examined are shown in table 2, where (L_x, L_y, H) are the domain dimensions in (x, y, z), l_K and τ_K are the Kolmogorov length and time scales, respectively, and wall units (denoted by superscript $+$) are scaled by the viscous length scale $\delta_v = \nu/U_*$, where U_* is the *a priori* estimate of the friction velocity, which is approximated as $U_* = \sqrt{\nu\partial_z\bar{u}} \sim \sqrt{\nu U_\infty/\delta}$.

Our decomposition of the flow is the same as that of Phillips (1970) and Wunsch (1970): we decompose the flow into a quiescent, hydrostatic background flow (denoted by the subscript 'H' variables in (2.29), (2.30) and (2.31), where $\boldsymbol{u}_H = 0$) and solve for anomalies from the background flow (the left-hand sides of (2.33), (2.34) and (2.35)) that, when summed with the background flow component, satisfy the no-slip (2.26) and adiabatic (2.27) boundary conditions at the wall imposed on the total flow. The nonlinear governing equations for the anomalies are

$$\partial_x u + \partial_y v + \partial_z w = 0, \tag{4.1}$$

$$d_t u = \frac{1}{Ro}v - \partial_x p + \frac{1}{Re_L}\left(\partial_{xx} + \partial_{yy} + \partial_{zz}\right)u + C^2 b + F(t), \tag{4.2}$$

$$d_t v = -\frac{1}{Ro}u - \partial_y p + \frac{1}{Re_L}\left(\partial_{xx} + \partial_{yy} + \partial_{zz}\right)v, \tag{4.3}$$

$$d_t w = -\partial_z p + \frac{1}{Re_L}\left(\partial_{xx} + \partial_{yy} + \partial_{zz}\right)w + C^2 b\cot\theta, \tag{4.4}$$

$$d_t b = \frac{1}{Pr\,Re_L}\left(\partial_{xx} + \partial_{yy} + \partial_{zz}\right)b, \tag{4.5}$$

where the anomalies u, v, w, p and b are defined by (2.33)–(2.35). The material derivative on the left-hand side of (4.5) contains nonlinear buoyancy anomaly advection terms as well as the terms describing the time rate of change of anomalous buoyancy, $-(u + w\cot\theta)$, by the advection of background buoyancy. Since the linear solutions for the oscillating laminar flow (Thorpe 1987; Baidulov 2010) contain only the advective terms corresponding to the background buoyancy advection, the laminar stratification oscillates from negative to positive and back again in a linear advection–diffusion balance. However, the boundary layer stratification can weaken, relative to the oscillating laminar stratification, if the vertical gradient of the nonlinear anomalous buoyancy advection in (4.5) is negative and dominates the vertical gradient of background buoyancy advection. Therefore, gradients of nonlinear anomalous buoyancy advection must continually

950 A4-10

overcome the restratifying tendency of background buoyancy advection (e.g. $u > 0$ corresponds to a local decrease in buoyancy as relatively heavy fluid is advected upslope) for weakened boundary layer stratification to persist.

The anomalies were computed using the MPI-parallel pseudo-spectral partial differential equation solver Dedalus (Burns *et al.* 2019) using 128^3 modes. A third-order, four-stage, implicit–explicit Runge–Kutta method derived by Ascher, Ruuth & Spiteri (1997) was used for temporal integration. Chebyshev polynomial bases of the first kind were employed for spatial discretization on a cosine grid in the wall-normal direction. Chebyshev polynomials permit the exact enforcement of the adiabatic wall-boundary condition ((2.27) minus the background component) on the buoyancy field and no-slip/impermeability wall-boundary conditions on the velocities ((2.26) minus the background component). The 3/2 rule dealiasing scheme is used not only for dealiasing the spatial modes online but also for dealiasing post-processed flow statistics.

At the maximum wall-normal extent of the domain, the boundary conditions at infinity (2.18), (2.19) and (2.28) were approximated for the anomalies as free-slip, impermeable conditions:

$$\partial_z u = \partial_z v = w = 0, \tag{4.6}$$

and an adiabatic condition on just the anomaly:

$$\partial_z b = 0, \tag{4.7}$$

such that the total flow buoyancy gradient at $z = H$ is the background buoyancy gradient in that direction.

Although the impermeability condition causes the reflection of internal waves that reach the upper boundary, the effects are assumed to be negligible because of the negligible amount of energy propagated by such high-wavenumber waves in low-Reynolds-number flow. Gayen & Sarkar (2010*a*) found that for flat-bottomed stratified oscillatory flow at larger-Reynolds-number flow ($Re = 1790$), the vertical wave energy flux is less than 1 % of the boundary layer dissipation and production rates. Indeed, small but non-zero dissipation rates of turbulent kinetic energy (TKE) were found near the upper boundary in some of the simulations, presumably from subharmonic parametric instability or other wave–wave instabilities because of the free-slip reflective upper boundary condition. However, 99.9 % of the shear production rate and dissipation rate occurred within one Ozmidov length of the wall ($L_O = \sqrt{\varepsilon/N^3}$, using the magnitude of the background stratification for N) at the lower boundary for all simulations.

A small amount of grid-scale noise was observed primarily in the x, y directions for $Re = 840$ cases. However, the wall-normal integrated TKE balances (figure 4) the residual of the right-hand-side TKE equation terms and the calculation of $\partial_t K$ matched to graphical accuracy, suggesting the grid-scale noise did not significantly alter energetics. The resolution of $\Delta x/l_K = \Delta y/l_K = 13.8, 18.0$ (table 2) was chosen by estimating the characteristic scale of $\varepsilon = O(10^{-10})$ m^2 s^{-3} *a priori* assuming fully developed steady turbulence that satisfies the law of the wall, even though law-of-the-wall turbulence was not anticipated because of the transitional Reynolds numbers prescribed. The *a priori* estimate $\varepsilon = O(10^{-10})$ m^2 s^{-3} roughly agrees with the majority of the corresponding *a posteriori* average dissipation rates shown in table 4, despite the false assumptions of the *a priori* estimate. Since the TKE equation closes to graphical accuracy and the instabilities investigated are laminar in origin, we anticipate that the results of this study will remain the same at higher resolution. However, the small amount of signal attenuation at the

Nyquist wavenumbers suggests that the shear production and dissipation rates may be slightly underestimated.

The initial conditions were specified as the sum of the steady component (Phillips 1970; Wunsch 1970), the oscillating component (Thorpe 1987) at time $t = 0$ and uniformly distributed white noise corresponding to buoyancy anomaly perturbations of magnitude 10^{-10} m s^{-2}. All of the simulations that exhibited turbulence (defined as wall-normal integrated production rates of TKE greater than 10^{-10} m^3 s^{-3}) did so within two oscillations.

The parameter regimes shown in table 1 qualitatively describe flows forced by the M_2 tide frequency, which is specified as $\omega = 1.4 \times 10^{-4}$ (rad s^{-1}, for a 12.4 h tide period) and the Coriolis parameter is specified as $f = 10^{-4}$ (rad s^{-1}). Much of the abyssal ocean is filled with Antarctic Bottom Water (AABW), characterized by temperatures near 0 °C and practical salinities of approximately 35 psu. At 0 °C and 35 psu, the kinematic viscosity is 1.8×10^{-6} m^2 s^{-1} (Chen *et al.* 1973; Talley 2011) and the thermal diffusivity is 1.4×10^{-7} m^2 s^{-1} (Thorpe 2007); thus $Pr \approx 13$ for AABW. We specify the kinematic viscosity as $\nu = 2 \times 10^{-6}$ m^2 s^{-1} in the relevant parameters in table 1 and $Pr = 1$ for simplicity. We approximate the background buoyancy frequency at mid-latitude abyssal depths as $N = 10^{-3}$ rad s^{-1} (Thurnherr & Speer 2003). Baroclinic tide amplitudes of $U_\infty \leqslant 0.01$ m s^{-1} in tidal models (Turnewitsch *et al.* 2013) agree with observations at the northwestern edge of the Sargasso Sea at 34°N 70°W (Tarbell *et al.* 1985; Nash *et al.* 2004). Global assessments of slope criticality suggest that the same region is characterized by subcritical, low-angle slopes. We also examine supercritical slopes for completeness. The prescribed non-dimensional parameters in table 1 were varied by only varying the velocity, $U_\infty = 0.01, 0.005$ m s^{-1} corresponding to the two Reynolds numbers, and the slope angle (shown in the rightmost column of table 1).

4.2. *Intermittent turbulent bursts*

The integrated TKE budget of each simulation was computed in order to distinguish the laminar and turbulent regimes and to quantify turbulence production mechanisms. The planar mean TKE is defined as

$$K(z, t) \equiv \tfrac{1}{2} \left(\overline{u'^2} + \overline{v'^2} + \overline{w'^2} \right), \tag{4.8}$$

where the planar mean operator and variable decomposition are defined:

$$\bar{\phi}(z, t) = \frac{1}{L_x L_y} \int_{-L_x/2}^{L_x/2} \int_{-L_y/2}^{L_y/2} \phi(y, z, t) \, \mathrm{d}y \, \mathrm{d}x, \tag{4.9}$$

$$\phi(x, y, z, t) = \bar{\phi}(z, t) + \phi'(x, y, z, t), \tag{4.10}$$

and ϕ is any of the anomalous variables defined by (2.33)–(2.35). The planar mean TKE evolution equation is

$$\partial_t K + \partial_z \mathcal{T} = \mathcal{P} + \mathcal{B} - \varepsilon. \tag{4.11}$$

The TKE transport term $\partial_z \mathcal{T}$ includes all TKE flux divergences (mean, turbulent, pressure, diffusion), which vanish upon wall-normal integration of (4.11). The rate production of TKE by mean shear is $\mathcal{P}$ (production in the sense that, generally, $\mathcal{P} > 0$), and it is defined

950 A4-12

as

$$\mathcal{P}(z, t) = -\overline{u'w'}\partial_z\bar{u} - \overline{v'w'}\partial_z\bar{v}, \tag{4.12}$$

$$\mathcal{P}_{13} = -\overline{u'w'}\partial_z\bar{u}, \tag{4.13}$$

$$\mathcal{P}_{23} = -\overline{v'w'}\partial_z\bar{v}. \tag{4.14}$$

The buoyancy flux $\mathcal{B}$ is typically downgradient ($\mathcal{B} < 0$ amidst $\partial_z\bar{b} > 0$ or $\mathcal{B} > 0$ amidst $\partial_z\bar{b} < 0$), in which case it represents the conversion of TKE into potential energy, and it is defined as

$$\mathcal{B}(z, t) = \overline{w'_\eta b'} = \overline{u'b'}\sin\theta + \overline{w'b'}\cos\theta, \tag{4.15}$$

$$\mathcal{B}_1 = \overline{u'b'}\sin\theta, \tag{4.16}$$

$$\mathcal{B}_3 = \overline{w'b'}\cos\theta \tag{4.17}$$

in the rotated reference frame (where $w_\eta = d_t\eta$ is the velocity in the vertical, not the wall-normal velocity w). Defined in this manner a downgradient buoyancy flux may be reversible. A reversible buoyancy flux may be thought of as a buoyancy flux that converts TKE into potential energy through stirring alone. Finally, the dissipation rate of TKE

$$\varepsilon(z, t) = \nu\left(\overline{(\partial_x u')^2} + \overline{(\partial_x v')^2} + \overline{(\partial_x w')^2} + \overline{(\partial_y u')^2} + \overline{(\partial_y v')^2}\right.$$
$$\left. + \overline{(\partial_y w')^2} + \overline{(\partial_z u')^2} + \overline{(\partial_z v')^2} + \overline{(\partial_z w')^2}\right) \tag{4.18}$$

is positive definite and therefore the last term of (4.11) is always a sink of TKE.

The laminar oscillating boundary layer buoyancy gradient is transient and evanescent; therefore, we seek an integral quantity to measure the stabilizing/destabilizing effects of the time-periodic laminar buoyancy gradient. We borrow the concept of boundary layer displacement thickness (Monin & Yaglom 1971) and apply it to transient bulk buoyancy gradients rather than momentum. We refer to this measure as the boundary layer stratification thickness, δ_s. If the total buoyancy field is not constant over small distance in the wall-normal direction z_1, then it can be approximated as constant over some distance z_0 from the wall, where z_0 is defined by

$$N^2 z_0 = \int_0^{z_1} \partial_z\tilde{b}\,\mathrm{d}z. \tag{4.19}$$

It follows that

$$\delta_s = z_1 - z_0 = \int_0^{z_1}\left(1 - \frac{\partial_z\tilde{b}}{N^2}\right)\mathrm{d}z. \tag{4.20}$$

Since $\partial_z\tilde{b} \to N^2$ as $z_1 \to \infty$ the integrand of (4.20) vanishes as $z_1 \to \infty$.

Figure 3 shows the geometric interpretation of (4.19). Here $\delta_s > 0$ and indicates that, in bulk, the oscillating laminar boundary layer stratification is less than the background stratification, and vice versa as the sign of the laminar boundary layer buoyancy gradient oscillates from negative to positive in the laminar flow solutions provided in Appendix A. The stratification thickness is positive when heavier fluid is advected over lighter fluid that has been impeded from flowing upslope by molecular friction at the boundary. Note that $\delta_s < 0$ for the laminar steady flow component solutions because the analytical solutions (Phillips 1970; Wunsch 1970) require steady positive bulk stratification near the boundary,
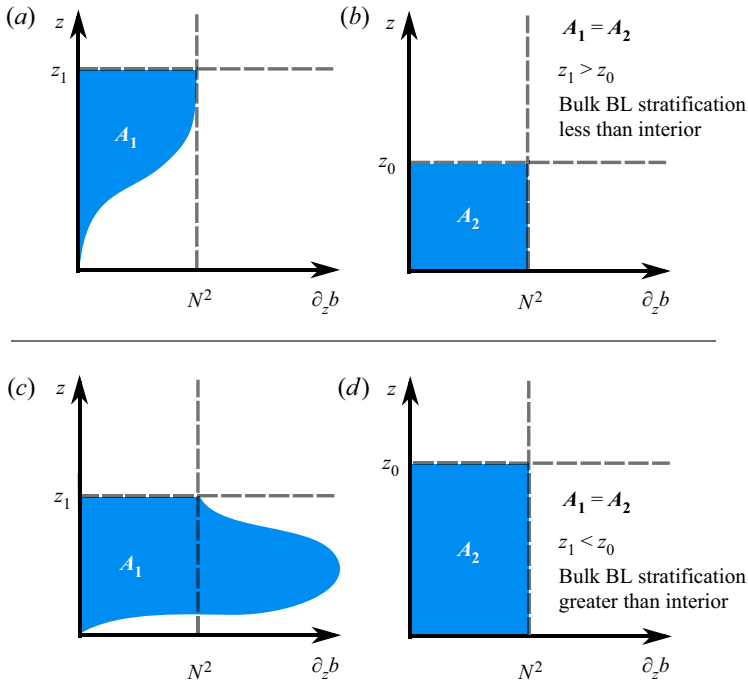
Figure 3. (*a–d*) Stratification thickness concept.

where isopycnals curve downwards. The stratification thickness was calculated for each flow investigated here, using the linear analytical solutions for the laminar oscillating flows and setting $z_1 \gg 1$.

The wave- and planar-averaged, wall-normal integrated TKE budget statistics for $Re = 840$ are shown in figure 4. The statistics were wave-averaged over 5–10 oscillations. All of the integrated TKE budgets at $Re = 840$, with the exceptions of case 5 and arguably case 7, possess a single burst of chaotic three-dimensional motion that is characterized by a rapid increase in the production rate of the TKE from the across-slope shear, $\mathcal{P}_{13}$, the component of shear parallel to the direction of the oscillating body force. The turbulent bursts, which occur shortly after $t/T \approx 0.5$, preferentially select the phase regime during which the velocity is upslope but decelerating, the sign of the oscillating buoyancy changes from positive to negative and the stratification thickness is negative (as indicated by the dark grey shading in figure 4). The negative stratification thickness preference of the bursts contrasts the low-Reynolds-number, intermittent turbulence regime of Stokes' second problem, in which a single burst occurs per oscillation, corresponding to the random selection of one of two shear maxima that occur within one period (Spalart & Baldwin 1987).

To investigate the role of the linear buoyancy dynamics in the formation of the turbulent bursts in figure 4, the time of the minimum total vertical buoyancy gradient in the linear solutions, which the reader may recall is negative for all of the considered parameter space as shown in figure 2, is depicted as the vertical dashed black line. The maximum TKE production rate by the mean shear approximately coincides in the time of the minimum total vertical buoyancy gradient for cases 1 and 6, the smallest intensity turbulent bursts shown in figure 4. The shear production is predominantly by $\mathcal{P}_{13}$, consistent with the notion that $w' > 0$ disturbances initiated by gravitational instabilities impede the mean
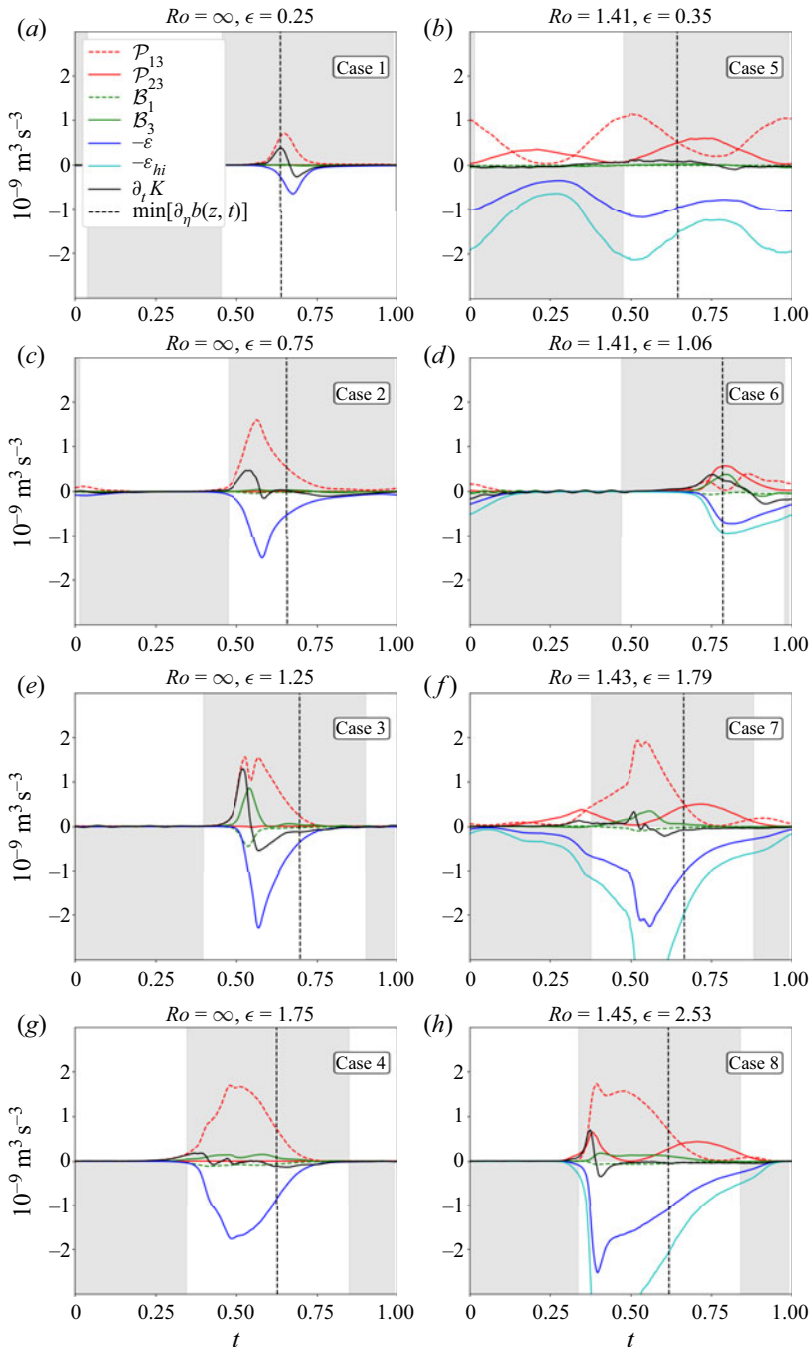
950 A4-14

Figure 4. (*a–h*) Wall-normal integrated, planar mean TKE budgets. The grey shading corresponds to the sign of the stratification thickness (negative (positive) represents enhanced (weak or negative) bulk boundary layer stratification). The dashed lines correspond to the time of the minimum total vertical buoyancy gradient in the linear solutions. The far-field velocity oscillates with $-\cos(t)$.

shear and trigger $u' < 0$. The negative Reynolds stresses combined with $\partial_z \bar{u} > 0$ during the upslope flow at $t \approx 0.5$ subsequently produce $\mathcal{P}_{13} > 0$ as plotted in figure 4. In the rotating cases, $\mathcal{P}_{23}$ is non-zero as mean shear in the along-isobath direction provides a source of TKE which is present in the non-rotating regime. This result suggests that the bursts of TKE production rate by the mean shear are triggered by buoyant ejections of low-momentum fluid upward. However, the triggering of buoyancy ejections is brief, weak and not sustained, because the buoyancy fluxes in figure 4 are negligible prior to bursts in the along-isobath shear production. Thus the gravitational instabilities appear to initiate, but not drive, bursts of chaotic three-dimensional motion.

It is well known that boundary layer turbulence is inherently anisotropic. However, the majority of ocean turbulence measurements measure the fluctuations of the vertical shear of the horizontal velocities and then assume homogeneous isotropic turbulent motion to subsequently estimate the dissipation rate (Polzin & Montgomery 1996; St. Laurent, Toole & Schmitt 2001). The isotropic, homogeneous turbulence dissipation rate of TKE (Taylor 1935) is defined in the sloped coordinate frame as

$$\varepsilon_{hi} = \tfrac{15}{4} \nu \cos^2 \theta \left(\overline{(\partial_z u')^2} + \overline{(\partial_z v')^2} \right). \tag{4.21}$$

The wall-normal integrated forms of ε_{hi} are plotted for the rotating reference frame cases in figure 4. Comparison of the dissipation rate assuming homogeneous isotropic turbulence (4.21) and the full dissipation rate (4.18), shown for the rotating cases, indicates that the assumption of homogeneous isotropic turbulence leads to overpredictions of the dissipation rate by a factor of approximately two. At high Reynolds number in unstratified boundary layers it is well known that the boundary layer dissipation rate is highly anisotropic in the viscous sublayer (Pope 2000); therefore we speculate that, if the Prandtl number remains unity, then the anisotropy of the dissipation rate will be similarly significant in the viscous sublayer of the high-Reynolds-number regimes of the flow investigated here.

4.3. *Gravitationally unstable rolls*

Except for case 6, all of the simulations at $Re = 840$ exhibited rolls characterized by growing streamwise vorticity. Figure 5 shows the instantaneous vertical velocity of case 2 to illustrate the life cycle of the rolls. In figure 5, red corresponds to upward motions and blue approximately corresponds to downward motions. The generation of two-dimensional convective rolls in the along-isobath/wall-normal (*y–z*) plane is visible just prior to the beginning of a burst. At time $t = 0.51$ the rolls appear and by $t = 0.55$ the rolls have begun to shear apart, erupting into the three-dimensional turbulence at the time of increase in TKE production by mean shear at $t = 0.55$.

The rolls formed by gravitational instabilities in figure 5 are qualitatively consistent with rolls observed in oscillating sloping stratified boundary layer experiments by Hart (1971). Hart (1971) identified spanwise plumes and rolls associated with the periodic reversals of the density gradient that qualitatively resembled the rolls that appeared in high-Rayleigh-number Couette flow experiments by Bénard & Avsec (1938), Chandra (1938) and Brunt (1951). Perhaps due to the similarity to the convection experiments, the rolls observed by Hart (1971) were referred to as 'convective rolls'. Linear stability analyses by Deardorff (1965), Gallagher & Mercer (1965) and Ingersoll (1966) revealed that the growth of gravitationally unstable disturbances in high-Rayleigh-number Couette flows is suppressed in the plane of the shear (the streamwise–vertical plane) by the shear (i.e. the suppression of the spanwise vorticity disturbances). They also found that the
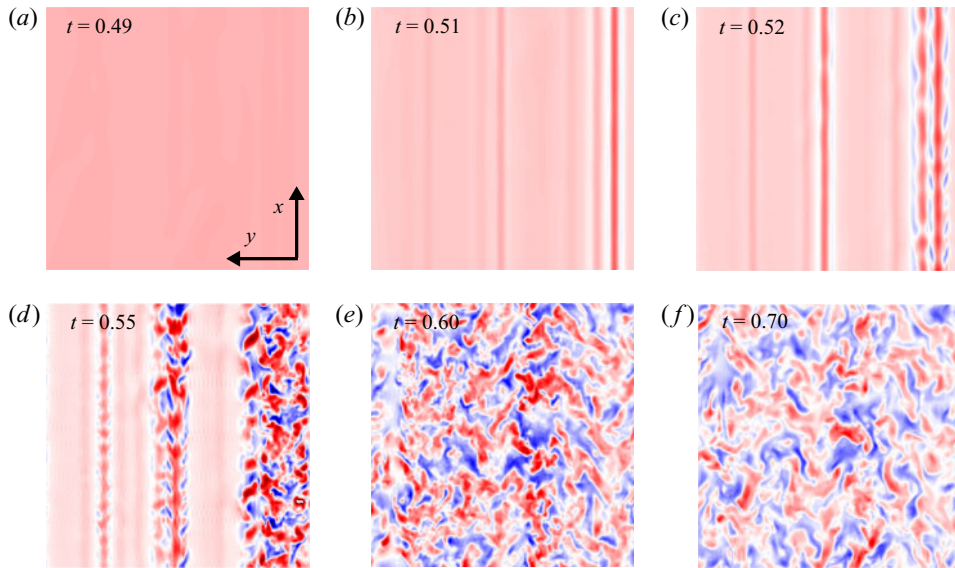
Figure 5. (*a*–*f*) Contours of the vertical velocity, w, for case 2. The contour plots show the vertical velocity at a fixed distance (roughly δ) in the wall-normal direction at six consecutive times. Here $w > 0$ is coloured red, while $w < 0$ is coloured blue. At $t = 0.5$ the across-isobath velocity is positive but begins to decelerate. Simultaneously, (*b*) two-dimensional rolls form in the y–z plane, as heavier fluid is advected over lighter fluid trapped near the wall by the friction.

growth of disturbances in the spanwise–vertical plane (steamwise vorticity disturbances) is unimpeded by the shear and grows in the same manner as pure convection. It has since been established that streamwise (the across-isobath direction) vortices with axes in the direction of a mean shear flow (or 'rolls') can arise due to heating or centrifugal effects (Hu & Kelly 1997). Linear stability analyses by Kaiser (2020) of the same regimes indicate that the streamwise (across-isobath) vorticity, which describes the rolls in figure 5, is linearly gravitationally unstable at the low Reynolds numbers investigated here. The initial growth of the rolls in figure 5 appears to have similar attributes.

To verify the hypothesis that gravitational instabilities spawn the rolls, which in turn spawn the turbulent burst, an additional simulation with the same parameters as those of case 2, but with the nonlinear advective terms in the buoyancy equation removed (i.e. replacing the material derivative $d_t\tilde{b}$ with $\partial_t\tilde{b}$ in (2.6)), was executed. The simulation of the non-advective buoyancy equation version of case 2 had no turbulent bursts over 10 cycles (all other simulations with bursts developed a burst within 2 cycles). The rolls are a bypass transition mechanism, lifting low-momentum fluid up and bringing high-momentum fluid down into the near-wall flow, and so they transiently destabilize the shear. The transient gravitationally unstable buoyancy gradients, discussed previously, can trigger oscillating boundary layer turbulent bursts even if the buoyancy fluxes are a negligible source of TKE.

Large-eddy simulation of a non-rotating internal wave beam at critical slope and at $Re = 10\,500$ ($U_\infty = 0.125$ m s^{-1}) by Gayen & Sarkar (2011) revealed turbulent bursts at the same time in the phase as those shown in figure 4: the bursts occur as the far-field velocity changes from downslope to upslope flow. However, the wall-normal structure of the prescribed internal wave beam investigated in Gayen & Sarkar (2011) produced turbulence dominated by buoyancy fluxes as the beam generated a much larger supply of potential energy through isopycnal tucking (dense water advected over light water) than is

possible by molecular diffusion. Given the differences in the magnitudes of the buoyancy fluxes in Gayen & Sarkar (2011) and those shown in figure 4, we speculate that the low- to transitional-Reynolds-number regime is characterized by shear-driven turbulent bursts triggered by gravitational instability, while the higher Reynolds number/smaller internal tide vertical wavelength regime is characterized by large buoyancy fluxes due to significant isopycnal tucking.

Although the streamwise rolls are initially two-dimensional, they produce a three-dimensional vorticity field. The inherent three-dimensionality of the gravitational instability is evident in the Boussinesq baroclinic production of vorticity term ($\nabla \times \tilde{b}$) in the absolute vorticity budget for rotating and non-rotating oscillating boundary layers:

$$\text{baroclinic production} = C^2 \big(\overbrace{\partial_y \tilde{b} \cot\theta \, \boldsymbol{i}}^{\substack{\text{nonlinear 2-D rolls} \\ \text{and 3-D bursts}}} + (\overbrace{\partial_x \tilde{b} \cot\theta}^{\substack{\text{nonlinear} \\ \text{3-D bursts}}} - \overbrace{\partial_z \tilde{b}}^{\substack{\text{linear flow} \\ \text{and 3-D bursts}}}) \boldsymbol{j} - \overbrace{\partial_y \tilde{b} \boldsymbol{k}}^{\substack{\text{nonlinear 2-D rolls} \\ \text{and 3-D bursts}}} \big). \quad (4.22)$$

The linear oscillating boundary layer vorticity field has only one vorticity component, the spanwise vorticity in the y direction, and the linear rotating oscillating boundary layer vorticity field is comprised of the spanwise vorticity and the streamwise vorticity in the x direction. In either case, only the $\partial_z \tilde{b} \boldsymbol{j}$ term in (4.22) is non-zero. However, the rolls produce gradients in the buoyancy field in the y direction. The first and last terms on the right-hand side of (4.22) indicate that the rolls in the y–z plane will inevitably generate vorticity in the streamwise and wall-normal directions; therefore, the rolls may induce three-dimensional motion in the oscillating boundary layers if viscosity and/or other mechanisms that suppress secondary instabilities are overcome. Therefore the coherent structures shown in figure 5, which facilitate the transition to turbulence, may initiate secondary instabilities through three-dimensional baroclinic production of vorticity, a phenomenon that is widely observed in other stratified shear flow instabilities (e.g. Peltier & Caulfield 2003).

4.4. *Relaminarization and instability suppression*

During the phase of enhanced boundary layer stratification relative to the background, $\delta_s < 0$ (the white regions in figure 4), the boundary shear instabilities must overcome not only the stabilizing effect of increased stratification but also the stabilizing effect of the wall that is present regardless of phase. Linear stability analysis by Schlichting (1935) yielded a critical gradient Richardson number of 1/24 for a stratified Blasius boundary layer, notably lower than the Miles–Howard theorem threshold for inviscid stratified shear. This suggests that the flow is stabilized with respect to shear perturbations during $\delta_s < 0$, although it is difficult to derive a suitable gradient Richardson number from the time-periodic boundary layer velocity and buoyancy solutions (Appendix A) because of inner and outer boundary layer gradients with opposite sign as well as shear and buoyancy gradient sign changes (figure 6). However, if the flow is turbulent during the phase of $\delta_s < 0$, turbulence model simulations at high Reynolds number by Umlauf & Burchard (2011) suggest mixing is much more efficient, presumably because the turbulence intensity required to overcome the strengthened boundary layer stratification must be considerable.

Three other mechanisms contribute to the relaminarization of the turbulent bursts in figure 4. First, the turbulent burst diffuses the mean shear and thus its primary energy source. Second, the tidal acceleration opposes the mean shear during the second half of the phase, so the decay and reversal of the shear amplitude imply that less mean flow kinetic energy is available. Third, once the flow reverses the outer boundary layer becomes
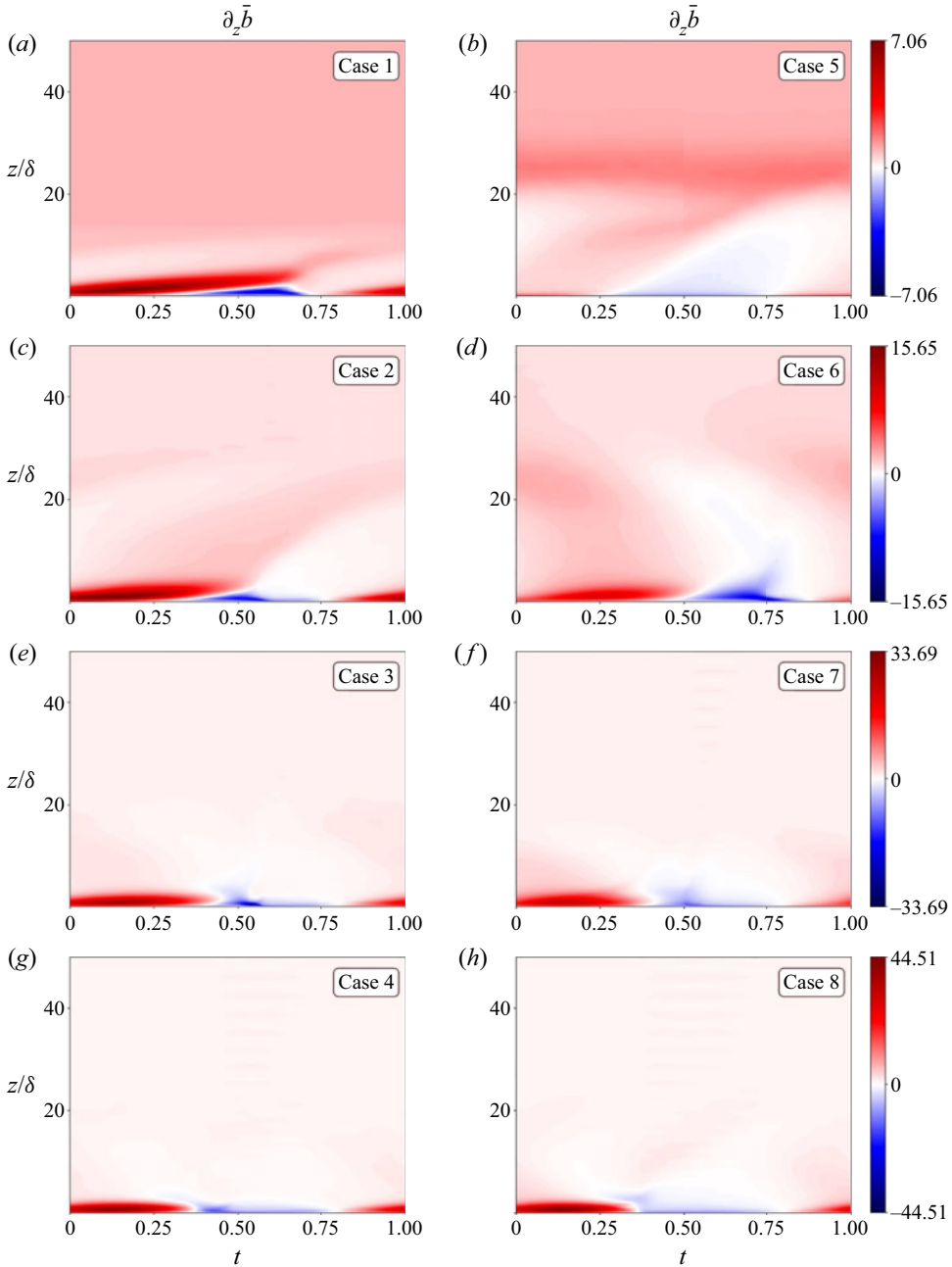
Figure 6. (*a–h*) Hövmuller plots of mean stratification for $Re = 840$. The total wall-normal buoyancy gradients are non-dimensionalized by N^2. The colour bar axes show that the boundary layer stratification maxima/minima increase/decrease with increasing slope.

increasingly stratified, as mentioned previously, when $\delta_s < 0$. For a burst to persist across the entire period it must have a constant source of mean shear of large enough magnitude to sustain production of TKE throughout flow reversals and increased stratification.

Case	Bu
5, 13	0.124
6, 14	1.127
7, 15	3.173
8, 16	6.347

Table 3. Rotating boundary layer simulation slope Burger numbers.

4.5. *The effect of rotation*

Only case 5 features sustained turbulence throughout the period (figure 4) and sustained boundary layer buoyancy homogenization (figure 6), because projection of the Coriolis force onto the wall-normal direction increases with decreasing slope, and thus oscillating Stokes–Ekman-like boundary layers develop at low angle. As the slope angle decreases, the boundary layer velocity spiral broadens in the along-isobath direction and mean shear is produced in the along-isobath direction, providing an additional source of TKE through a component of shear production, $\mathcal{P}_{23}$, that is not active in the non-rotating cases (figure 4). The Burger number is the ratio of the squares of the inertial period to the time scale associated with the buoyant restoring force. The slope Burger number accounts for the rotated reference frame, defined as

$$Bu = Ro^2 C^2 = \frac{N^2 \tan^2 \theta}{f^2}. \tag{4.23}$$

If $Bu < 1$, the buoyant restoring force acts more slowly than the Coriolis force and rotation is significant. Table 3 shows the Burger number for the rotating boundary layer flows, cases 5–8 and 13–16. Cases of the lowest slope Burger number, cases 5 and 13, are influenced the most by rotation. In case 5, the highest-Reynolds-number and lowest-Burger-number flow, the turbulence is sustained throughout the period and the mean velocity field oscillates in a tidal ellipse. These results suggest that, within the investigated parameter regime, low-Burger-number flows are more likely to sustain turbulence throughout the entire period because the tidal ellipse of the boundary layer mean shear can supply TKE even at times in the oscillation when the component of mean shear in the across-isobath direction is weak.

4.6. *Barotropic tide dissipation*

In oceanography, the rate of energy loss to drag per square metre of the barotropic flow by tidal bottom boundary layers is often estimated using the quasi-empirical model $D \approx \rho_0 c_D |U| U^2$ (Hoerner 1965), where c_D is the dimensionless drag coefficient and U is an estimate of the bulk velocity (Jayne & St. Laurent 2001; St. Laurent & Garrett 2002). The rate of energy dissipated by the tide can be represented in terms of watts per metre squared by

$$D \approx \rho_0 \int_0^{30\delta} \bar{\varepsilon} \, \mathrm{d}z, \tag{4.24}$$

where $\bar{\varepsilon}$ is the dimensional time mean dissipation rate of TKE (units $\mathrm{m^2\ s^{-3}}$). Lacking a time-mean length scale for the boundary layer thickness that applies to bursting flows, we spatially average the dissipation rate of TKE over the region of 5 m near the wall, equivalent to averaging over approximately $0 < z < 30\delta$. For flat-plate boundary layers,

Case	Re	c_D	ε_{BL}	$(L_O/L_K)^{4/3}$
1	840	1.8×10^{-4}	3.5×10^{-11}	1.8×10^{1}
2	840	9.7×10^{-4}	1.9×10^{-10}	9.6×10^{1}
3	840	1.6×10^{-3}	3.2×10^{-10}	1.6×10^{2}
4	840	3.5×10^{-3}	6.9×10^{-10}	3.5×10^{2}
5	840	4.7×10^{-3}	9.3×10^{-10}	4.6×10^{2}
6	840	5.1×10^{-4}	1.0×10^{-10}	5.0×10^{1}
7	840	5.0×10^{-3}	9.9×10^{-10}	4.9×10^{2}
8	840	5.4×10^{-3}	1.1×10^{-9}	5.3×10^{2}
9	420	8.8×10^{-5}	2.2×10^{-12}	1.1×10^{0}
10	420	~ 0	~ 0	~ 0
11	420	~ 0	~ 0	~ 0
12	420	~ 0	~ 0	~ 0
13	420	~ 0	~ 0	~ 0
14	420	1.6×10^{-8}	3.9×10^{-16}	2.0×10^{-4}
15	420	1.5×10^{-3}	3.7×10^{-11}	1.8×10^{-1}
16	420	1.4×10^{-3}	3.4×10^{-11}	1.7×10^{-1}

Table 4. Drag coefficients, averaged dissipation rates and Ozmidov–Kolmogorov length-scale ratios estimated from time-mean simulation results.

the transitional flow regime is characterized by drag coefficients in the range $0.001 \leqslant c_D \leqslant 0.005$, for $1 < Re < 10^3$ or equivalently $1 < Re_L < 10^6$ (Hoerner 1965). The drag coefficients for the low-Reynolds-number boundary layers in this study were calculated as

$$c_D = \frac{D}{\rho_0 U_\infty^3}. \tag{4.25}$$

The drag coefficients are shown in table 4. The drag coefficient values shown in table 4 mostly fall within the expected range for flat-plate boundary layers, with the exception of the steepest slope case at $Re = 840$, case 8. The drag coefficients are small at $Re = 420$ for all but the steepest slope angles in the rotating reference frame (cases 15 and 16). In table 4, ~ 0 represents negligible drag. The drag coefficients increase with slope at constant Reynolds number, and they effectively vanish in a portion of the range $420 < Re < 840$ on lower slopes where the flow is in the laminar or disturbed laminar abyssal slope regime.

The average boundary layer dissipation rates ε_{BL} and the ratio of Ozmidov to Kolmogorov length scales $(L_O/L_K)^{4/3}$ are also shown in table 4, where

$$\varepsilon_{BL} \approx \frac{1}{30\delta} \int_0^{30\delta} \bar{\varepsilon} \, dz, \tag{4.26}$$

$$\left(\frac{L_O}{L_K}\right)^{4/3} = \frac{\varepsilon_{BL}}{\nu N^2}. \tag{4.27}$$

The use of the ratio of Ozmidov to Kolmogorov length scales L_O/L_K to characterize the bulk effect of stratification on turbulence can be traced to the isotropy parameter of Gargett, Osborn & Nasmyth (1984). More recently, Gargett's ratio raised to the 4/3 power has been referred to as the isotropy parameter I (Thorpe 2007; Ivey, Winters & Koseff 2008) and as the buoyancy Reynolds number Re_b (Ivey *et al.* 2021; Mashayek *et al.* 2022). To avoid confusion, we refer to Gargett's ratio raised to the 4/3 power as the Ozmidov–Kolmogorov length-scale ratio.

Sign changes in the oscillating boundary layer buoyancy gradient (see figure 6 and the buoyancy solutions for the laminar flow provided in Appendix A) and therefore it does not lend itself to a simple time-mean estimate of the buoyancy gradient; therefore, the background buoyancy gradient N^2 is used in (4.27). Since the Ozmidov–Kolmogorov length-scale ratio does not distinguish between weak stratification and strong turbulence, the $O(100)$ values presented in table 4 should be interpreted as weak turbulence, or chaotic motions with little scale separation that overcome weaker stratification. The dissipation rates presented in table 4 are consistent with observed minimum abyssal dissipation rates of $\varepsilon \sim 10^{-10}$ m^2 s^{-3} (Thorpe 2007). The low levels of dissipation rate and the relaminarization of the turbulent bursts imply that in all but the sustained turbulence case (case 5) the irreversible buoyancy flux is negligible. However, $I > 100$ in stratified homogeneous turbulence is associated with significant irreversible buoyancy fluxes in laboratory experiments (Shih *et al.* 2005; Ivey *et al.* 2008), suggesting (1) that a better estimation of the characteristic boundary layer buoyancy gradient is required and (2) that the interpretation of the Ozmidov–Kolmogorov length-scale ratio near adiabatic boundaries is ambiguous because $(L_O/L_K)^{4/3} \rightarrow \infty$ on a steady adiabat.

5. Conclusions

We investigated transition pathways of low-Reynolds-number, oscillating, stratified, diffusive boundary layers on infinite slopes in rotating and non-rotating reference frames on extra-critical slopes. Our results suggest that the laminar boundary layers are destabilized by a two-dimensional gravitational instability, characterized by the formation of rolls aligned axially in the across-isobath direction, which triggers bursts of turbulence that are supplied with energy from the mean shear. This phenomenon occurred for all of the investigated parameter space, except for low slope Burger number ($Bu \leqslant 1/8$) and for cases of low Reynolds number and low slope angle ($Re = 420$, $\theta < 0.1$). The low-slope-angle, low-Reynolds-number cases remained laminar. The low-slope-Burger-number, $Re \approx 840$, case is qualitatively similar to stratified Stokes–Ekman layers, and it was the only simulation that exhibited sustained boundary layer buoyancy homogenization, or 'mixing'. In that case, steady shear-driven turbulence throughout the period continually eroded the stratification ($\mathcal{P}_{13}$ and $\mathcal{P}_{23}$ in figure 4), even during the downslope phase when light buoyancy anomalies advected downslope increase the stratification and suppress motion in the boundary layer (figure 6).

Vertically integrated TKE budgets suggest that energy supply to the transient turbulent bursts ($Re \approx 840$ flows except for case 5 in figure 4) was extracted from the mean shear. Increasing the slope parameter ϵ resulted in increases in turbulent burst intensity, quantified by integrated TKE shear production, and to a much lesser degree also induced larger positive turbulent buoyancy fluxes. The positive turbulent buoyancy fluxes eroded negative buoyancy gradients and generated downgradient buoyancy diffusion. The turbulent bursts in rotating reference frames (slope $Ro = 1.4$) were qualitatively similar to the non-rotating reference frame bursts.

During the phase of downslope mean flow the bursts where observed to relaminarize. With the exception of $Bu \leqslant 1/8$ (case 5), we observed that the boundary layer stratification significantly controls the transitional and intermittent regimes within $420 \lesssim Re \lesssim 840$ by suppressing turbulence during the downslope flow phase and triggering TKE production by the mean shear during the upslope flow phase.

Bulk estimates of the maximum boundary layer Rayleigh number (see figure 2) from analytical solutions were consistent with gravitational instabilities that were observed

in simulations of varying parameter space. The gravitational instabilities for rolls qualitatively resemble the convective rolls of diabatic Couette flow (Ingersoll 1966), and the correlation between the timing of their formation and gravitationally unstable stratification in the boundary layer suggests that the instabilities are characterized by the upward ejection of buoyant low-momentum fluid near the wall which acts similarly to near-wall ejections in unstratified flows by initiating shear production (Robinson 1991). Our results agree with Floquet linear instability of the laminar flow solutions (Kaiser 2020) that the boundary layers investigated are susceptible to linear gravitational instabilities at low Reynolds number.

The dissipation rates of TKE and drag coefficients increased with increased slope parameter, more for the non-rotating cases than the rotating cases. The drag coefficients (table 4) become negligibly small as the Reynolds number is decreased because, below $Re \approx 840$, the oscillating boundary layer is laminar and thus the time-mean drag is negligible, $D \approx 0$. The drag coefficients at $Re = 840$ increased with slope angle. The time-mean boundary layer Ozmidov–Kolmogorov length-scale ratio $(L_O/L_K)^{4/3} = \varepsilon/(\nu N^2)$ was found to be elevated in some cases despite the low levels of turbulence mixing. However, both the definition of a time-mean buoyancy gradient for a boundary layer with time-periodic buoyancy gradient sign changes and the meaning of the Ozmidov–Kolmogorov length-scale ratio near an adiabatic boundary are ambiguous.

The idealized flows investigated here are different from 'tranquil region' abyssal slopes, such as can be found at 34°N 70°W, in several ways. First, we set the Prandtl number to unity, whereas in § 4.1 we observed that a plausible abyssal value of the Prandtl number for AABW is $Pr \approx 13$. We speculate that $Pr > 1$ will increase the role of gravitational instabilities from merely triggering shear-driven turbulent bursts to the production of significant buoyancy fluxes. Second, we investigated steep slope angles, which are not characteristic of the continental slopes or other large-horizontal-scalebathymetric features. However, the results shown here may be relevant to shorter-horizontal-scale bathymetric features (e.g. abyssal hills of 10 km horizontal scale) if the boundary oscillation has negligible variability over $O(10)$ m scales. Despite these differences, the dissipation rates of TKE are consistent with background abyssal dissipation rates of $\varepsilon \sim O(10^{-10})$ m^2 s^{-3} (Thorpe 2007), and the drag coefficient of case 5 (low slope Burger number, $Re = 840$, arguably the most characteristic case of mid-latitude tranquil regions in the abyss) is similar to the drag coefficient found in significantly more turbulent boundary layers on the continental shelf (Zulberti, Jones & Ivey 2020), suggesting that $c_D \sim O(10^{-3})$ is potentially applicable to disparate oceanic boundary layers across a broad range of Re. Further investigation is needed to assess the role of increased Pr, higher Re, hydraulic roughness and other phenomena that occur on extra-critical slopes in the abyssal ocean.

Declarations of interests. The authors report no conflict of interest.

Author ORCIDs.
Ⓓ Bryan E. Kaiser https://orcid.org/0000-0002-4652-6935.

Appendix A

The following is a derivation of the solutions to (A2), (A3) and (A4). In the other sections of this paper, partial derivatives are denoted by ∂_{zz} for the second derivative in z, for example. In this appendix, Leibniz notation is used for derivatives. We begin by assuming linear oscillating solutions of the form

$$u_{O,d} = \mathcal{U}(z)\mathrm{e}^{\mathrm{i}\omega t}, \quad v_{O,d} = \mathcal{V}(z)\mathrm{e}^{\mathrm{i}\omega t}, \quad b_{O,d} = \mathcal{B}(z)\mathrm{i}\mathrm{e}^{\mathrm{i}\omega t}, \tag{A1a–c}$$

where d denotes the variables are dimensional and O denotes the oscillating components (2.29) and (2.31). It does not matter if we make the ansatz $\mathcal{V}(z)\mathrm{e}^{\mathrm{i}\omega t}$ or $\mathcal{V}(z)\mathrm{i}\mathrm{e}^{\mathrm{i}\omega t}$ (the latter is the correct final form) because the particular solution fixes the phase relationship of u and v. The oscillating components of the dimensional and linearized forms of (2.2)–(2.6), with no variation in the across-isobath (x) or along-isobath (y) directions, satisfy

$$\partial_t u_{O,d} = f v_{O,d} + \nu \partial_{zz} u_{O,d} + b_{O,d} \sin\theta + F_d(t), \tag{A2}$$

$$\partial_t v_{O,d} = -fu + \nu \partial_{zz} v_{O,d}, \tag{A3}$$

$$\partial_t b_{O,d} = -u_{O,d} N^2 \sin\theta + \kappa \partial_{zz} b_{O,d}, \tag{A4}$$

where the wall-normal momentum vanishes by conservation of mass and the wall-normal momentum equation again reduces to a diagnostic equation for the pressure field. Substitution of the ansatz (A1a–c) into the linearized governing equations (A2), (A3) and (A4) yields

$$\left(\mathrm{i}\omega - \nu\frac{\partial^2}{\partial z^2}\right)\mathcal{U} = \mathcal{V}f\cos\theta + \mathrm{i}\mathcal{B}\sin\theta + A\mathrm{i}, \tag{A5}$$

$$\left(\mathrm{i}\omega - \nu\frac{\partial^2}{\partial z^2}\right)\mathcal{V} = -\mathcal{U}f\cos\theta, \tag{A6}$$

$$\left(\mathrm{i}\omega - \kappa\frac{\partial^2}{\partial z^2}\right)\mathrm{i}\mathcal{B} = -\mathcal{U}N^2\sin\theta. \tag{A7}$$

The equations above can be reduced to a single inhomogeneous linear partial differential equation for the wall-normal buoyancy structure $\mathcal{B}(z)$:

$$\left[\left(\mathrm{i}\omega - \nu\frac{\partial^2}{\partial z^2}\right)\left(\mathrm{i}\omega - \nu\frac{\partial^2}{\partial z^2}\right)\left(\mathrm{i}\omega - \kappa\frac{\partial^2}{\partial z^2}\right) + N^2\sin^2\theta\left(\mathrm{i}\omega - \nu\frac{\partial^2}{\partial z^2}\right)\right.$$
$$\left. - f^2\cos^2\theta\left(\mathrm{i}\omega - \kappa\frac{\partial^2}{\partial z^2}\right)\right]\mathrm{i}\mathcal{B} = A\omega N^2\sin\theta. \tag{A8}$$

Equation (A8) has six characteristic roots for the complementary (homogeneous) component of the solution and six linearly independent solutions. To obtain the characteristic solutions, we expand all of the terms in (A8):

$$\left(\frac{\partial^6}{\partial z^6} - \mathrm{i}\left(\frac{2\omega}{\nu} + \frac{\omega}{\kappa}\right)\frac{\partial^4}{\partial z^4} + \left(-\frac{\omega^2}{\nu^2} - \frac{2\omega^2}{\nu\kappa} + \frac{f^2\cos^2\theta}{\nu^2} + \frac{N^2\sin^2\theta}{\nu\kappa}\right)\frac{\partial^2}{\partial z^2}\right.$$
$$\left. + \mathrm{i}\left(-\frac{f^2\cos^2\theta\omega}{\nu^2\kappa} - \frac{N^2\sin^2\theta\omega}{\nu^2\kappa} + \frac{\omega^3}{\nu^2\kappa}\right)\right)\mathcal{B} = \mathrm{i}\frac{A\omega N^2\sin\theta}{\nu^2\kappa}. \tag{A9}$$

Therefore the non-homogeneous ordinary differential equation has the form

$$\left(\frac{\partial^6}{\partial z^6} + \mathrm{i}a_4 \frac{\partial^4}{\partial z^4} + a_2 \frac{\partial^2}{\partial z^2} + \mathrm{i}a_0 \right) \mathcal{B} = \mathrm{i}f_p, \tag{A10}$$

where the subscript p denotes 'particular solution' and

$$\left. \begin{aligned} a_4 &= -\left(\frac{2\omega}{\nu} + \frac{\omega}{\kappa} \right) = -\frac{\omega}{\kappa} \left(\frac{2}{Pr} + 1 \right) = -\frac{\omega}{\kappa} \left(\frac{2+Pr}{Pr} \right), \\ a_2 &= -\frac{\omega^2}{\nu^2} - \frac{2\omega^2}{\nu\kappa} + \frac{f^2 \cos^2 \theta}{\nu^2} + \frac{N^2 \sin^2 \theta}{\nu\kappa} = \frac{f^2 \cos^2 \theta + PrN^2 \sin^2 \theta - \omega^2(1+2Pr)}{\kappa^2 Pr^2}, \\ a_0 &= \frac{\omega^3}{\nu^2 \kappa} - \frac{f^2 \cos^2 \theta \omega}{\nu^2 \kappa} - \frac{N^2 \sin^2 \theta \omega}{\nu^2 \kappa} = \frac{\omega(\omega^2 - f^2 \cos^2 \theta - N^2 \sin^2 \theta)}{\kappa^3 Pr}, \\ f_p &= \frac{A\omega N^2 \sin \theta}{\nu^2 \kappa}. \end{aligned} \right\} \tag{A11}$$

Equation (A10) has the characteristic equation

$$\lambda^6 + \mathrm{i}a_4 \lambda^4 + a_2 \lambda^2 + \mathrm{i}a_0 = 0, \tag{A12}$$

which has six distinct solutions for λ. The total general solution is the sum of the complementary (homogeneous) solutions and the particular (non-homogeneous) solutions:

$$\mathcal{B}(z) = \mathcal{B}_C(z) + \mathcal{B}_p(z). \tag{A13}$$

The complementary solution is therefore of the form

$$\mathcal{B}_C(z) = c_1 \mathrm{e}^{\lambda_1} + c_2 \mathrm{e}^{\lambda_2} + c_3 \mathrm{e}^{\lambda_3} + c_4 \mathrm{e}^{\lambda_4} + c_5 \mathrm{e}^{\lambda_5} + c_6 \mathrm{e}^{\lambda_6} \tag{A14}$$

and the particular part of the solution is of the form

$$\mathcal{B}_p = a_p, \tag{A15}$$

where a_p is an unknown constant.

A.1. *The particular solution*

To solve for a_p, we substitute the particular solution form (A15) into the non-homogeneous governing equation (A10):

$$\begin{aligned} a_p &= \frac{f_p}{a_0} \\ &= \frac{AN^2 \sin \theta}{\omega^2 - f^2 \cos^2 \theta - N^2 \sin^2 \theta}. \end{aligned} \tag{A16}$$

A.2. *The complementary solution*

Let $\phi = \lambda^2$ in (A12) to obtain

$$\phi^3 + \mathrm{i}a_4 \phi^2 + a_2 \phi + \mathrm{i}a_0 = 0, \tag{A17}$$

950 A4-25

where

$$\lambda_{1,2} = \pm\sqrt{\phi_1}, \quad \lambda_{3,4} = \pm\sqrt{\phi_2}, \quad \lambda_{5,6} = \pm\sqrt{\phi_2}. \tag{A18a–c}$$

The solutions to this equation are

$$\beta = \sqrt[3]{2\mathrm{i}a_4^3 + 9\mathrm{i}a_2a_4 + 3\sqrt{3}\sqrt{4a_2^3 + a_4^2a_2^2 + 18a_0a_4a_2 + 4a_0a_4^3 - 27a_0^2 - 27\mathrm{i}a_0}}, \tag{A19}$$

$$\phi_1 = \frac{\beta}{3\sqrt[3]{2}} - \frac{\sqrt[3]{2}\left(a_4^2 + 3a_2\right)}{3\beta} - \frac{\mathrm{i}a_4}{3}, \tag{A20}$$

$$\phi_2 = -\frac{\left(1 - \mathrm{i}\sqrt{3}\right)\beta}{6\sqrt[3]{2}} + \frac{\left(1 + \mathrm{i}\sqrt{3}\right)\left(a_4^2 + 3a_2\right)}{3\cdot 2^{2/3}\beta} - \frac{\mathrm{i}a_4}{3}, \tag{A21}$$

$$\phi_3 = -\frac{\left(1 + \mathrm{i}\sqrt{3}\right)\beta}{6\sqrt[3]{2}} + \frac{\left(1 - \mathrm{i}\sqrt{3}\right)\left(a_4^2 + 3a_2\right)}{3\cdot 4^{1/3}\beta} - \frac{\mathrm{i}a_4}{3}. \tag{A22}$$

A.3. *Boundary conditions*

For the parameter space we are interested in $c_1 = c_3 = c_5 = 0$ (to have finite solutions at $z = \infty$):

$$\mathcal{B}(z) = c_2\mathrm{e}^{-\sqrt{\phi_1}z} + c_4\mathrm{e}^{-\sqrt{\phi_2}z} + c_6\mathrm{e}^{-\sqrt{\phi_3}z} + a_p. \tag{A23}$$

Now we reinterpret the boundary conditions in terms of $\mathcal{B}$:

(i) No slip at the wall ($z = 0$) applied to the across-slope velocity

$$\mathcal{U} = -\frac{1}{N^2\sin\theta}\left(\mathrm{i}\omega - \kappa\frac{\partial^2}{\partial z^2}\right)\mathrm{i}\mathcal{B} = 0 \tag{A24}$$

leads to the expression

$$c_2(\omega + \mathrm{i}\kappa\phi_1) + c_4(\omega + \mathrm{i}\kappa\phi_2) + c_6(\omega + \mathrm{i}\kappa\phi_3) = -a_p\omega. \tag{A25}$$

(ii) No slip at the wall ($z = 0$) applied to the along-slope velocity

$$\mathcal{V} = \frac{1}{f\cos\theta}\left(\frac{1}{N^2\sin\theta}\left(\omega^2 + \mathrm{i}\omega(\nu + \kappa)\frac{\partial^2}{\partial z^2} - \nu\kappa\frac{\partial^4}{\partial z^4}\right)\mathcal{B} - \sin\theta\mathcal{B} - A\right) = 0 \tag{A26}$$

leads to the expression

$$\begin{aligned}
c_6(\mathrm{i}\omega\phi_3(\kappa + \nu) &- \kappa\nu\phi_3^2 - N^2\sin^2\theta + \omega^2) \\
&+ c_2\left(\mathrm{i}\omega\phi_1(\kappa + \nu) - \kappa\nu\phi_1^2 - N^2\sin^2\theta + \omega^2\right) \\
&+ c_4\left(\mathrm{i}\omega\phi_2(\kappa + \nu) - \kappa\nu\phi_2^2 - N^2\sin^2\theta + \omega^2\right) \\
&= AN^2\sin\theta - a_p\left(\omega^2 - N^2\sin^2\theta\right).
\end{aligned} \tag{A27}$$

(iii) The adiabatic wall boundary condition

$$\frac{\partial \mathcal{B}}{\partial z} = 0 + 0\mathrm{i} \quad \text{at } z = 0 \tag{A28}$$

leads to the expression

$$- c_4\sqrt{\phi_2} - c_6\sqrt{\phi_3} - c_2\sqrt{\phi_1} = 0. \tag{A29}$$

Therefore we can solve for the coefficients. In matrix form:

$$\boldsymbol{E} \cdot \boldsymbol{x} = \boldsymbol{y} \tag{A30}$$

or

$$\begin{bmatrix} E_{11} & E_{12} & E_{13} \\ E_{21} & E_{22} & E_{23} \\ E_{31} & E_{32} & E_{33} \end{bmatrix} \begin{bmatrix} x_1 \\ x_2 \\ x_3 \end{bmatrix} = \begin{bmatrix} y_1 \\ y_2 \\ y_3 \end{bmatrix}, \tag{A31}$$

where we solve for

$$x_1 = c_2 = b_1, \quad x_2 = c_4 = b_2, \quad x_3 = c_6 = b_3, \tag{A32a–c}$$

with $\boldsymbol{E}$ and $\boldsymbol{y}$ specified by the boundary conditions:

$$y_1 = -a_p \omega, \quad y_2 = AN^2 \sin\theta - a_p\left(\omega^2 - N^2 \sin^2\theta\right), \quad y_3 = 0, \tag{A33a–c}$$

$$\left.\begin{aligned}
E_{11} &= \omega + \mathrm{i}\kappa\phi_1, \quad E_{12} = \omega + \mathrm{i}\kappa\phi_2, \quad E_{13} = \omega + \mathrm{i}\kappa\phi_3, \\
E_{21} &= \mathrm{i}\omega\phi_1(\kappa + \nu) - \kappa\nu\phi_1^2 - N^2 \sin^2\theta + \omega^2, \\
E_{22} &= \mathrm{i}\omega\phi_2(\kappa + \nu) - \kappa\nu\phi_2^2 - N^2 \sin^2\theta + \omega^2, \\
E_{23} &= \mathrm{i}\omega\phi_3(\kappa + \nu) - \kappa\nu\phi_3^2 - N^2 \sin^2\theta + \omega^2, \\
E_{31} &= -\sqrt{\phi_1}, \quad E_{32} = -\sqrt{\phi_2}, \quad E_{33} = -\sqrt{\phi_3}.
\end{aligned}\right\} \tag{A34}$$

The solutions for the coefficients in the $\mathcal{B}$ solution (see (A32a–c)) are

$$\begin{aligned}
\Upsilon &= \kappa^2\nu(\sqrt{\phi_2\phi_3}\phi_1 + \sqrt{\phi_1\phi_3}\phi_2 + \sqrt{\phi_1\phi_2}\phi_3) \\
&\quad + \mathrm{i}\kappa\nu\omega(\sqrt{\phi_1\phi_2} + \sqrt{\phi_1\phi_3} + \sqrt{\phi_2\phi_3} + \phi_1 + \phi_2 + \phi_3) \\
&\quad + \nu\omega^2 + \kappa N^2 \sin^2\theta,
\end{aligned} \tag{A35}$$

$$\begin{aligned}
b_1 &= -\frac{1}{\left(\sqrt{\phi_1} - \sqrt{\phi_2}\right)\left(\sqrt{\phi_1} - \sqrt{\phi_3}\right)\Upsilon} \Big(A\kappa N^2\sqrt{\phi_2\phi_3}\sin\theta + \mathrm{i}AN^2\omega\sin\theta \\
&\quad + \kappa N^2 a_p\sqrt{\phi_2\phi_3}\sin^2\theta + \mathrm{i}\kappa\nu a_p\omega(\sqrt{\phi_3}\phi_2^{3/2} + \phi_3\phi_2 + \sqrt{\phi_2}\phi_3^{3/2}) + \nu a_p\omega^2\sqrt{\phi_2\phi_3}\Big),
\end{aligned} \tag{A36}$$

$$b_2 = \frac{1}{\left(\sqrt{\phi_1} - \sqrt{\phi_2}\right)\left(\sqrt{\phi_2} - \sqrt{\phi_3}\right)\Upsilon} \left(A\kappa N^2 \sqrt{\phi_1\phi_3}\sin\theta + iAN^2\omega\sin\theta\right.$$
$$\left. + \kappa N^2 a_p \sqrt{\phi_1\phi_3}\sin^2\theta + i\kappa v a_p\omega(\sqrt{\phi_3}\phi_1^{3/2} + \phi_3\phi_1 + \sqrt{\phi_1}\phi_3^{3/2}) + v a_p\omega^2\sqrt{\phi_1\phi_3}\right),$$
$$\text{(A37)}$$

$$b_3 = -\frac{1}{\left(\sqrt{\phi_1} - \sqrt{\phi_3}\right)\left(\sqrt{\phi_2} - \sqrt{\phi_3}\right)\Upsilon} \left(A\kappa N^2 \sqrt{\phi_1\phi_2}\sin\theta + iAN^2\omega\sin\theta\right.$$
$$\left. + \kappa N^2 a_p \sqrt{\phi_1\phi_2}\sin^2\theta + i\kappa v a_p\omega(\sqrt{\phi_2}\phi_1^{3/2} + \phi_2\phi_1 + \sqrt{\phi_1}\phi_2^{3/2}) + v a_p\omega^2\sqrt{\phi_1\phi_2}\right).$$
$$\text{(A38)}$$

A.4. *Solutions*

The solutions for the oscillating component of the flow (the components with subscript '*O*' in (2.29) and (2.30)) are

$$b_{O,d}(z,t) = \text{Re}\left[\mathcal{B}(z)\text{e}^{i\omega t}\right] = \text{Re}\left[\left(c_2\text{e}^{-\sqrt{\phi_1}z} + c_4\text{e}^{-\sqrt{\phi_2}z} + c_6\text{e}^{-\sqrt{\phi_3}z} + a_p\right)\text{e}^{i\omega t}\right],$$
$$\text{(A39)}$$

where b_1, b_2 and b_3 are given by (A36), (A37) and (A38). The across-slope velocity coefficients are

$$u_1 = b_1(\omega + i\kappa\phi_1), \tag{A40}$$
$$u_2 = b_2(\omega + i\kappa\phi_2), \tag{A41}$$
$$u_3 = b_3(\omega + i\kappa\phi_3), \tag{A42}$$

and the along-slope velocity coefficients are

$$v_1 = b_1(i\omega\phi_1(\kappa + v) - \kappa v\phi_1^2 - N^2\sin^2\theta + \omega^2), \tag{A43}$$
$$v_2 = b_2(i\omega\phi_2(\kappa + v) - \kappa v\phi_2^2 - N^2\sin^2\theta + \omega^2), \tag{A44}$$
$$v_3 = b_3(i\omega\phi_3(\kappa + v) - \kappa v\phi_3^2 - N^2\sin^2\theta + \omega^2), \tag{A45}$$

and the velocity solutions are

$$u_{O,d}(z,t) = \text{Re}\left[\mathcal{U}(z)\text{e}^{i\omega t}\right]$$
$$= \text{Re}\left[\frac{\left(u_1\text{e}^{-\sqrt{\phi_1}z} + u_2\text{e}^{-\sqrt{\phi_2}z} + u_3\text{e}^{-\sqrt{\phi_3}z} + a_p\omega\right)\text{e}^{i\omega t}}{N^2\sin\theta}\right], \tag{A46}$$

$$v_{O,d}(z,t) = \text{Re}\left[\mathcal{V}(z)\text{e}^{i\omega t}\right]$$
$$= \text{Re}\left[\frac{\left(v_1\text{e}^{-\sqrt{\phi_1}z} + v_2\text{e}^{-\sqrt{\phi_2}z} + v_3\text{e}^{-\sqrt{\phi_3}z} + a_p(\omega^2 - N^2\sin^2\theta) - AN^2\sin\theta\right)\text{ie}^{i\omega t}}{fN^2\cos\theta\sin\theta}\right]. \tag{A47}$$

References

ANGEL, M.V. 1990 Life in the benthic boundary layer: connections to the mid-water and sea floor. *Phil. Trans. R. Soc. Lond.* A **331** (1616), 15–28.

ASCHER, U., RUUTH, S. & SPITERI, R. 1997 Implicit-explicit Runge–Kutta methods for time-dependent partial differential equations. *Appl. Numer. Maths* **25** (2), 151–167.

BAIDULOV, V. 2010 Fine structure of one-dimensional periodic stratified flows. *Fluid Dyn.* **45** (6), 835–842.

BALMFORTH, N., IERLEY, G. & YOUNG, W. 2002 Tidal conversion by subcritical topography. *J. Phys. Oceanogr.* **32** (10), 2900–2914.

BECKER, J. & SANDWELL, D. 2008 Global estimates of seafloor slope from single-beam ship soundings. *J. Geophys. Res.* **113** (C5), C05028.

BELL, T. 1975*a* Lee waves in stratified flows with simple harmonic time dependence. *J. Fluid Mech.* **67**, 705–722.

BELL, T. 1975*b* Topographically generated internal waves in the open ocean. *J. Geophys. Res.* **80**, 320–327.

BÉNARD, H. & AVSEC, D. 1938 Travaux récents sur les tourbillons cellulaires et les tourbillons en bandes. Applications à l'astrophysique et à la météorologie. *J. Phys. Radium* **9** (11), 486–500.

BRUNT, D. 1951 Experimental cloud formation. In *Compendium of Meteorology*, pp. 1255–1262. Springer.

BURNS, K., VASIL, G., OISHI, J., LECOANET, D. & BROWN, B. 2019 Dedalus: a flexible framework for numerical simulations with spectral methods. arXiv:1905.10388.

CHANDRA, K. 1938 Instability of fluids heated from below. *Proc. R. Soc. Lond.* A **164** (917), 231–242.

CHANDRASEKHAR, S. 1961 *Hydrodynamic and Hydromagnetic Stability*. Oxford University Press.

CHEN, S., CHAN, R., READ, S. & BROMLEY, L. 1973 Viscosity of sea water solutions. *Desalination* **13** (1), 37–51.

DAVIS, S. 1976 The stability of time-periodic flows. *Annu. Rev. Fluid Mech.* **8** (1), 57–74.

DEARDORFF, J. 1965 Gravitational instability between horizontal plates with shear. *Phys. Fluids* **8** (6), 1027–1030.

FERRARI, R., MASHAYEK, A., MCDOUGALL, T., NIKURASHIN, M. & CAMPIN, J. 2016 Turning ocean mixing upside down. *J. Phys. Oceanogr.* **46** (7), 2239–2261.

GALLAGHER, A.P. & MERCER, A.McD., 1965 On the behaviour of small disturbances in plane Couette flow with a temperature gradient. *Proc. R. Soc. Lond.* A **286** (1404), 117–128.

GARGETT, A., OSBORN, T. & NASMYTH, P. 1984 Local isotropy and the decay of turbulence in a stratified fluid. *J. Fluid Mech.* **144**, 231–280.

GARRETT, C. & KUNZE, E. 2007 Internal tide generation in the deep ocean. *Annu. Rev. Fluid Mech.* **39**, 57–87.

GAYEN, B. & SARKAR, S. 2010*a* Large eddy simulation of a stratified boundary layer under an oscillatory current. *J. Fluid Mech.* **643**, 233–266.

GAYEN, B. & SARKAR, S. 2010*b* Turbulence during the generation of internal tide on a critical slope. *Phys. Rev. Lett.* **104** (21), 218502.

GAYEN, B. & SARKAR, S. 2011 Boundary mixing by density overturns in an internal tidal beam. *Geophys. Res. Lett.* **38** (14), L14608.

HART, J. 1971 A possible mechanism for boundary layer mixing and layer formation in a stratified fluid. *J. Phys. Oceanogr.* **1**, 258–262.

HOERNER, S. 1965 Fluid-dynamic drag. *Hoerner Fluid Dynamics*.

HU, H. & KELLY, R. 1997 Stabilization of longitudinal vortex instabilities by means of transverse flow oscillations. *Phys. Fluids* **9** (3), 648–654.

INGERSOLL, A. 1966 Convective instabilities in plane Couette flow. *Phys. Fluids* **9** (4), 682–689.

IVEY, G.N., WINTERS, K.B. & KOSEFF, J.R. 2008 Density stratification, turbulence, but how much mixing? *Annu. Rev. Fluid Mech.* **40**, 169–184.

IVEY, G.N., BLUTEAU, C.E., GAYEN, B., JONES, N.L. & SOHAIL, T. 2021 Roles of shear and convection in driving mixing in the ocean. *Geophys. Res. Lett.* **48** (3), e2020GL089455.

JAYNE, S. & ST. LAURENT, L., 2001 Parameterizing tidal dissipation over rough topography. *Geophys. Res. Lett.* **28** (5), 811–814.

KAISER, B.E. 2020 Finescale abyssal turbulence: sources and modeling. PhD thesis, Massachusetts Institute of Technology.

MASHAYEK, A., BAKER, L.E., CAEL, B.B. & CAULFIELD, C.P. 2022 A marginal stability paradigm for shear-induced diapycnal turbulent mixing in the ocean. *Geophys. Res. Lett.* **49** (2), e2021GL095715.

MONIN, A. & YAGLOM, A. 1971 *Statistical Fluid Dynamics*, vol. 1. MIT.

NASH, J.D., KUNZE, E., TOOLE, J.M. & SCHMITT, R.W. 2004 Internal tide reflection and turbulent mixing on the continental slope. *J. Phys. Oceanogr.* **34** (5), 1117–1134.

PELTIER, W. & CAULFIELD, C. 2003 Mixing efficiency in stratified shear flows. *Annu. Rev. Fluid Mech.* **35** (1), 135–167.

PHILLIPS, O. 1970 On flows induced by diffusion in a stably stratified fluid. *Deep-Sea Res.* **17** (3), 435–443.

POLZIN, K. 1996 Statistics of the Richardson number: mixing models and finestructure. *J. Phys. Oceanogr.* **26** (8), 1409–1425.

POLZIN, K. & MONTGOMERY, E. 1996 Microstructure profiling with the high resolution profiler. In *Proceedings of the Office of Naval Research Workshop on Microstructure Sensors*, pp. 109–115.

POPE, S. 2000 *Turbulent Flows*. Cambridge University Press.

ROBINSON, S.K. 1991 Coherent motions in the turbulent boundary layer. *Annu. Rev. Fluid Mech.* **23** (1), 601–639.

SARKAR, S. & SCOTTI, A. 2017 From topographic internal gravity waves to turbulence. *Annu. Rev. Fluid Mech.* **49**, 195–220.

SCHLICHTING, H. 1935 Hauptaufsätze: turbulenz bei wärmeschichtung. *Z. Angew. Math. Mech.* **15** (6), 313–338.

SHIH, L.H, KOSEFF, J.R, IVEY, G.N & FERZIGER, J.H 2005 Parameterization of turbulent fluxes and scales using homogeneous sheared stably stratified turbulence simulations. *J. Fluid Mech.* **525**, 193–214.

SPALART, P. & BALDWIN, B. 1987 Direct simulation of a turbulent oscillating boundary layer. In *Turbulent Shear Flows 6*, pp. 417–440. Springer.

ST. LAURENT, L. & GARRETT, C. 2002 The role of internal tides in mixing the deep ocean. *J. Phys. Oceanogr.* **32** (10), 2882–2899.

ST. LAURENT, L., TOOLE, J. & SCHMITT, R. 2001 Buoyancy forcing by turbulence above rough topography in the Abyssal Brazil Basin. *J. Phys. Oceanogr.* **31** (12), 3476–3495.

TALLEY, L. 2011 *Descriptive Physical Oceanography*. Academic.

TARBELL, S.A., MONTGOMERY, E.T. & BRISCOE, M.G. 1985 A compilation of moored current meter and wind recorder data. *Tech. Rep.* Woods Hole Oceanographic Institution.

TAYLOR, G. 1935 Statistical theory of turbulence. *Proc. R. Soc. Lond.* A **151** (873), 421–444.

THORPE, S. 1987 Current and temperature variability on the continental slope. *Phil. Trans. R. Soc. Lond.* A **323**, 471–517.

THORPE, S. 2007 *An Introduction to Ocean Turbulence*. Cambridge University Press.

THURNHERR, A. & SPEER, K. 2003 Boundary mixing and topographic blocking on the Mid-Atlantic Ridge in the South Atlantic. *J. Phys. Oceanogr.* **33** (4), 848–862.

TURNEWITSCH, R., FALAHAT, S., NYCANDER, J., DALE, A., SCOTT, R. & FURNIVAL, D. 2013 Deep-sea fluid and sediment dynamics—influence of hill- to seamount-scale seafloor topography. *Earth Sci. Rev.* **127**, 203–241.

UMLAUF, L. & BURCHARD, H. 2011 Diapycnal transport and mixing efficiency in stratified boundary layers near sloping topography. *J. Phys. Oceanogr.* **41** (2), 329–345.

WUNSCH, C. 1970 On oceanic boundary mixing. *Deep-Sea Res.* **17** (2), 293–301.

ZULBERTI, A., JONES, N.L. & IVEY, G.N. 2020 Observations of enhanced sediment transport by nonlinear internal waves. *Geophys. Res. Lett.* **47** (19), e2020GL088499.